12-17-2004

A Novel Chirp Slope Keying Modulation Scheme for Underwater Communication

Lastri Simanjuntak
University of New Orleans

A NOVEL CHIRP SLOPE KEYING MODULATION SCHEME FOR UNDERWATER COMMUNICATION

A Thesis

Submitted to the Graduate Faculty of the
University of New Orleans
in partial fulfillment of the
requirements for the degree of

Master of Science
in
The Department of Electrical Engineering

by

Lastri L. E. Simanjuntak

B.S., University of New Orleans

December 2004

ACKNOWLEDGMENTS

First of all, I would like to express my gratitude to my thesis advisor Dr. Bourgeois for her continuous attention, guidance, and support through out the duration of this thesis. This research could not be possible without her.

I also would like to thank my thesis committee members Dr. Riemer, Dr. Charalampidis, and Mr. Jovanovich for their suggestions and insightful comments.

I would like to give special thank to my friends. I am very grateful for their continuous moral support and for their friendships. I wish to also thank my family in Golden Meadow for their love and support throughout the years.

Finally, and above all, my greatest appreciation goes to God and my family, whose love and great support was indispensable, and who have provided me with prayers, lifetime motivation and inspiration.

ABSTRACT

A digital modulation method using Chirp-Slope Keying (CSK) is developed for coherent underwater acoustic communications. Effective signal detection is a critical stage in the implementation of any communications system; we will see that CSK solves some significant challenges to reliable detection. This thesis is primarily based on analyzing the effectiveness of CSK through simulations using Matlab's Simulink for underwater communications. The procedure begins with modulating a chirp's slope by random binary data with a linear-down-slope chirp representing a 0, and a linear-up-slope chirp representing a 1. Each received symbol is demodulated by multiplying it with the exact linear-up-slope chirp and then integrating over a whole period (i.e., integrate and dump). This slope-detection technique reduces the need for the extensive recognition of the magnitude and/or the frequencies of the signal. Simulations demonstrate that CSK offers sturdy performance in the modeled ocean environment, even at very low signal-to-noise ratio (SNR).

CSK is first tested using the fundamental communication channel, Additive White Gaussian Noise (AWGN) channel. Simulation results show excellent BER vs. SNR performance, implying CSK is a promising method. Further extensive analysis and simulations are performed to evaluate the quality of CSK in more realistic channels including Rayleigh amplitude fading channel and multipath.

TABLE OF CONTENTS

LIST OF FIGURES

LIST OF TABLES

1. INTRODUCTION

1.1 THE PROBLEM OF UNDERWATER COMMUNICATION

The simplest and basic way of establishing communication between two remote underwater sites is by using cable connected between a receiver and a transmitter. However, this method has several disadvantages: it is expensive, maintenance and repair are difficult especially if the communication takes place in the deep water, and the drag from the cable can be a problem if the user is small and mobile. Furthermore, it is practically impossible in most situations to connect a receiver and transmitter this way.

Another way of establishing communication between two remote underwater sites is by using water as the medium to propagate the signal. The most common underwater wireless communication channel is the UWA channel – Underwater Acoustic Channel. However, the UWA channel is quite possibly nature's most unforgiving wireless communication medium. From a communication perspective, the UWA channel creates many challenges to the realization of reliable, high data rate, and long distance communications. There are many physical characteristics of the water channel and their effects on the communication problems that have lead to a slow growth of underwater wireless communication technology.

The general main issues of concern in the UWA channel are the combined effects of severe bandwidth limitation and the physical characteristics of the underwater channel. These issues lead to a fundamental tradeoff between data rate and reliability. There are

four aspects of the UWA channel that are of primary concern: ambient noise, transmission loss due to geometrical spreading and absorption, reverberation due to multipath, and Doppler spreading due to relative motion. Each must be considered in modeling the appropriate UWA channel [1 - 3].

Ambient noise is caused by man-made activities, sea life, and waves. The noise levels are very site-dependent, especially in shallow water. Generally the onshore environments, such as marine work-sites or ports, are much noisier than the deep ocean. Ambient noise influences the signal-to-noise ratio which ultimately constrains the data transmission rate for a given probability error (PE) or decreases accuracy for a given rate.

Transmission loss is caused by energy spreading and sound absorption. The absorption loss occurs due to energy lost to heat in the water. This loss increases with both frequency and range. It is a primary factor in determining the maximum usable frequency, hence the available bandwidth for a particular range.

The most challenging aspect of the UWA channel is the reverberation due to multipath propagation. The mechanism of multipath formation is dependent on the location within the ocean: deep water or shallow water. It is also dependent on the frequency and range of transmission. Two main mechanisms of multipath formation are the reflection at the water boundaries (bottom, surface, and any objects in the water), and ray bending. Multipath propagation contributes to signal fading, and causes inter-symbol interference (ISI) in digital communication systems. In the past, this multipath propagation resulted in restricting communication in the UWA channel to noncoherent modulation schemes, and low data rates [1].

Doppler spreading is one implication of relative motion between the transmitter and receiver or by ocean internal factors (such as water motion in the channel). Some

shift motion can be compensated for, for example if the motion is slowly varying due to ship motion. However, random motion manifests a continuous spreading that is more difficult to compensate for.

1.2 BACKGROUND AND LITERATURE REVIEW

Underwater communication technology can be traced back to its roots several centuries to its fundamental discoveries. Toward the end of the fifteenth century, Leonardo da Vinci wrote in his notes [4]:

> *"If you cause your ship to stop, and place the head of a long tube in the water and place the outer extremity to your ear, you will hear ships at a great distance from you."*

This acknowledgement includes all the essential elements of a modern passive sonar system. Da Vinci recognized that moving ships generate sound in the water that may propagate to considerable distances. He describes the long tube placed between the water and the ear as the receiving device.

In the more recent past, underwater acoustic communications have received much attention, mostly by the military, associated with submarines detection. The initial application of acoustic technology was during World War I, and continued through World War II until the end of the Cold War. Many institutions were formed to study underwater communications (e.g. Naval Electronics Laboratory at San Diego and the Woods Hole Oceanographic Institution).

In recent years, the applications of underwater acoustic communications are beginning to shift from military towards commercial applications. Today, underwater communication systems are employed in various unmanned submersibles (e.g. robots, underwater vehicles (ROV's)) which are replacing divers in a variety of offshore work

tasks. The remaining major constraint is the limited capability of underwater communication systems. Currently, there are six relevant research areas [5]: 1) underwater channel physics, channel simulations, and measurements; 2) receiver structures; 3) diversity exploitation; 4) error control coding; 5) networked systems; and 6) alternative modulation strategies. This thesis primarily discusses an alternate modulation strategy using Chirp-Slope Keying.

Modeling the underwater channel accurately has a very important role in obtaining accurate characterization of an optimal communications system. Many recent works have focused on channel characterization and modeling [1-3, 5-8]. Because of the difficulties in accurately characterizing the statistical behavior of underwater acoustic channels, tolerance to uncertain statistical modeling is important. Because of the nonhomogeneous, nonstationary, and non-Gaussian nature of the underwater acoustic channels, it is necessary to adopt techniques other than those suggested by the classical theory. According to [8], two of the most pervasive approaches to this problem are adaptive processing and nonparametric processing. Another class of techniques that can be used to process signals in uncertain statistical underwater environments is the so-called robust method – or uncertainty tolerance. Similarly, [7] also presents a detailed analytical overview of underwater acoustic channel modeling and threshold signal processing. Middleton emphasized the inhomogeneous, random, and non-Gaussian nature of the generalized channel, combined with appropriate weak-signal detection and estimation. He primarily focuses on to the structuring of the scattered and ambient acoustic noise fields. However, he only intends to present a general guide to the formulation and treatment of specific propagation and signal processing problems.

As mentioned in section 1.1, sound propagation underwater is primarily constrained by ambient noise, transmission loss, reverberation – multipath propagation, and Doppler spreading. For high data rates on time-spread multipath propagation channels, one approach to signal design which avoids the effects of multipath is the use of frequency shift keying (FSK) or phase shift keying (PSK) [9]. Most recently, noncoherent demodulation has generally been preferred because of the phase instabilities caused by the Doppler spreading [10, 11]. Spread spectrum techniques have been considered for resolving these problems [12] because spread spectrum can make effective use of bandwidth and tolerate large distortion. This includes chirp-slope keying (CSK).

1.3 SPREAD SPECTRUM COMMUNICATIONS

Spread spectrum signals have been proposed for communication systems to resist multipath, decorrelate impulsive noise, resist jamming interference, and to provide some immunity to frequency selective fading [12]. Spread spectrum systems are those where the transmitted signal is spread over a wide frequency range, wider than the transmitted information itself. The formal definition of spread spectrum [27]:

> *"Spread spectrum is an RF communications system in which the baseband signal bandwidth is intentionally spread over a larger bandwidth by injecting a higher-frequency signal. As a direct consequence, energy used in transmitting the signal is spread over a wider bandwidth, and appears as noise. The ratio (in dB) between the spread baseband and the original signal is called processing gain. Typical SS processing gains run from 10dB to 60dB."*

To be classified as spread spectrum, the modulated signal bandwidth should be at least 10 to 100 times wider than the information rate [13].

Spread spectrum systems can be divided into four general types of modulation: direct sequence (DS), frequency hopping (FH), time hopping (TH), and pulse-FM or

chirp modulation (CM). There are also various hybrid combinations of modulation forms, such as FH/DS modulation and TH/DS modulation, to name a few.

Direct sequence (DS) modulated systems use modulation of a carrier by a digital code sequence where the bit rate is much higher than the information signal bandwidth. The result of modulating with such a code sequence is to produce a DS modulated spread spectrum with $\left(\sin x / x\right)^2$ frequency spectrum, centered at the carrier frequency.

Frequency hopping (FH) modulation is based on old-fashioned frequency shift keying (FSK), except that the set of frequency choices is greatly expanded. The carrier frequency is hopped or shifted in discrete increments from frequency to frequency in a code sequence pattern. The speed at which the shifts are executed depends on the data rate of the original information.

Time hopping (TH) modulation uses a code sequence to trigger a transmitter to be on and off. The difference between FH and TH is that in FH systems the transmitted frequency is changed at each code bit time, whereas TH systems may change frequency only at the one/zero transitions in the code sequence.

One type of spread spectrum modulation that does not necessarily employ coding but uses a wide bandwidth is chirp modulation (CM). The carrier of CM is swept over a wide band during a given pulse interval. Most CM systems use a linear sweep pattern.

1.4 CHIRP MODULATION BACKGROUND

Analog chirp signals or linear frequency modulation signals have been used extensively in radar technology and, more recently, in sonar systems. Chirp modulation is one of the older spread spectrum methods which was developed for radar use in the

mid-1940s [14, 15]. The basic idea is to transmit long frequency modulated pulses in which the frequency changes continuously in one direction (increasing or decreasing) without reversal for the duration of the pulse.

Chirp signals in digital communications were seemingly originally[1] suggested by Winkler in 1962 [16]. The idea is to use a pair of linear chirps that have opposite chirp rates for binary signaling. Winkler proposed chirp signal because of its high robustness against distortions and different types of interference. In [17], binary chirp signal, or what Berni called linear frequency sweeping (LFS), is compared to FSK and PSK in coherent, partially coherent, and fading channels (Rayleigh and Rician channel models). Berni found that LFS is superior to FSK with 1.3 dB improvement in terms of required signal energy and bandwidth for a given probability error in coherent channels. In non-coherent channels, LFS is less appealing because of the requirement for a phase recovery system. In non-selective slow fading channels, the relatively simpler implementation of FSK rules out the use of LFS for orthogonal signaling. However, theoretically, chirp signal has superior characteristics in the partially coherent and fading cases, for certain rangers of channel conditions.

The use of chirp modulation for multiple access was first proposed by Cook in 1974 [18]. He proposed the use of chirp signals hopping different modulation slopes and different bandwidths for multiple-user applications. El-Khamy extended Cook's approach to improve performance in [19-22]. This suggested technique was motivated by the inherent interference rejection capability of such spread-spectrum type systems,

---

[1] We found this reference after extensive searches. The current author and the advisor developed CSK independently (vita 2001) before encountering [16].

especially in circumstances where immunity against Doppler shift and fading due to multipath propagation is important. Simulation results show that chirp modulation spread spectrum may be efficient and promising as a multiple access technique. In 2002, Hengstler extended Cook's and El-Khamy's approach for efficient and flexible multiple access using the new chirp modulation spread spectrum (CMSS) [13, 28]. The BER results show good agreement between theory and simulation. Comparing with other spread spectrum systems, Hengstler's new CMSS outperforms the existing chirp modulation technique and BER performance attainable by direct sequence spread spectrum systems.

In recent years, more authors have researched and utilized chirp signals in communications systems. [23, 24] use a chirp FSK modem for high reliability communications in shallow water. Fifty six narrowband chirp FSK pulses, each centered at a unique frequency in the range of 20 kHz to 30 kHz, are used. The communication rates vary from 300 bps to 2400 bps. An improved modem, by LeBlanc, uses 56 narrowband chirp FSK pulses, each centered at a unique frequency in the range of 16 kHz to 32 kHz. The communication rates vary from 221 bps to 1172 bps. Experiments show that the system is virtually insensitive to selective fading, reverberation, and Doppler.

In this thesis, simple linear-up and linear-down chirp signals are used to represent binary 0 and 1, respectively. Simulations show that even with only a first order filter, the system shows an excellent BER performance. Our system may be easily expanded to represent higher order modulation by increasing the number of up and down chirps.

1.5 THESIS OUTLINE

This thesis is organized into four major chapters. Chapter 2 explains in more detail the basic underwater channel models. It describes four major deleterious underwater channel effects: ambient noise, transmission loss, reverberation, and double spread (time and Doppler). Chapter 2 also describes the statistical channel models use in our simulations. The main objective of this thesis is addressed in Chapter 3. In this chapter, the theoretical and general properties of chirp-slope keying modulation (CSK) are analyzed. Chapter 4 provides simulation results in four different statistical underwater channel models. Finally, Chapter 5 summarizes the results presented in this thesis and gives suggestions for possible future studies.

2. UNDERWATER CHANNEL MODELS

In order to be able to perform underwater acoustic communication, it is important to understand what happens to the signal on its way from the transmitter to the receiver. Knowledge of the physical properties of the underwater medium is crucial. Also, understanding the physics of signal propagation plays a key role in designing communication systems. Thus, in this chapter, the main issues of concern in underwater communication channels, mentioned in Section 1.1, will be discussed: ambient noise, transmission loss due to geometrical scattering and absorption, reverberation due to multipath, and Doppler spreading due to relative motion. Ambient noise and transmission loss are the principal limitations for the available signal-to-noise ratio [1], while reverberation and Doppler spreading influences signal design and processing, often imposing severe limitations on system performance [3].

2.1 AMBIENT NOISE IN THE OCEAN

There are many different kinds of acoustic signals in the ocean; some of them are noiselike in character. The term ambient noise refers to the noise that remains after all identifiable sound sources are eliminated. The sources of ambient noise are both natural (e.g. seismic disturbance, agitation of the sea surface by wind, biological sources) and human-made (e.g. distant shipping, ship traffic). The levels of ambient noise are highly

dependent on geographic location, acoustic transmission characteristics, season of the year, and weather.

Ambient noise can be divided into three bands. The low-frequency band covers the range from 1Hz up to several hundred Hz. The ambient noise in this band is dominated by the sounds of distant shipping and seismic activity. However, this very low frequency region is generally not of great interest in the design of underwater acoustic systems. The mid-frequency band covers the range from several hundred Hz up to 50 KHz. In this band, the ambient noise is dominated by the effects of wind acting on the sea surface. The ambient noise level in this band increases approximately 5 dB for every doubling of wind speed. The high-frequency band covers everything above 50 KHz. The ambient noise in this band is dominated by the thermal agitation of the water molecules. The noise level in this band increases at a rate of approximately 6 dB per octave as frequency increases. Typical ambient noise spectra for the three bands discussed are shown in Figure 2.1 [2]

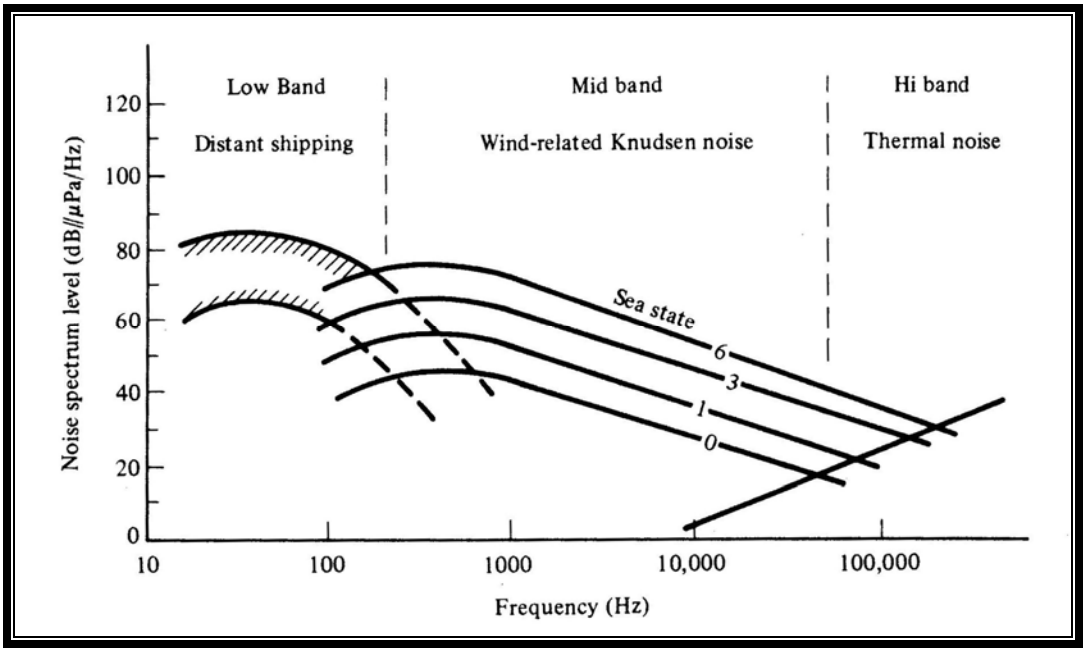

Figure 2.1 – Typical deep water ambient noise spectra [2]

Ambient noise can be modeled statistically as the variation of the noise field in space and time because the ambient noise is a random process. This process is non-stationary in space and time. However, for simplicity the ambient noise process is usually assumed to be stationary in both space and time. The degree to which stationarity assumptions are valid depends on the application.

Ambient noise influences the signal to noise ratio (SNR) which ultimately constraints the data transmission rate versus reliability tradeoff. Ambient noise level decreases with frequency. Figure 2.2 illustrates typical power density spectral distribution for ambient noise in the ocean [3].

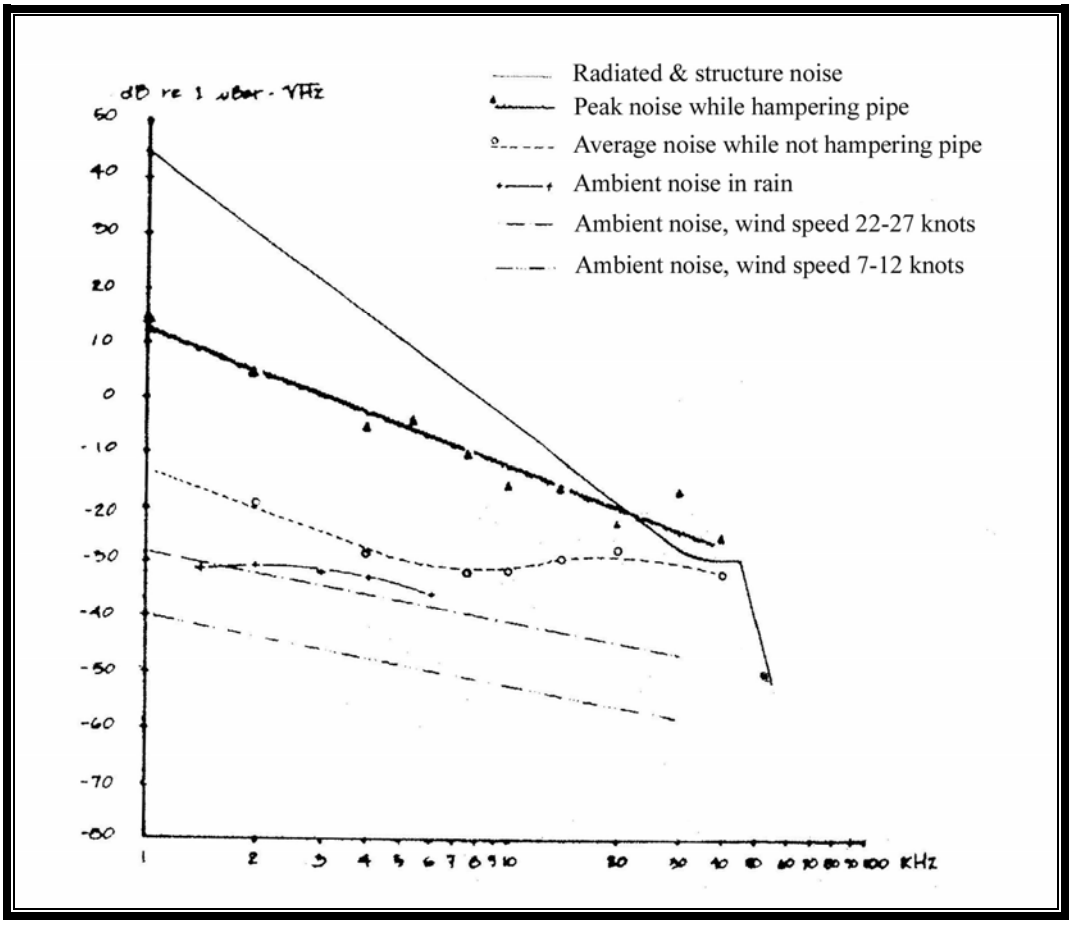

Figure 2.2 – Ambient noise in man made and natural environments in the ocean [3]

2.2 SOUND TRANSMISSION IN THE OCEAN

The sound transmission characteristics in the UWA channel are extremely complex. Sound speed is primarily a function of temperature, depth, and salinity. Temperature is a function of depth, time, location, and weather conditions. The ocean surface varies from smooth to very rough and turbulent surface that scatters sound randomly. The ocean bottom has a wide variety of compositions, slopes, and roughnesses. All these effects determine the characteristics of acoustic transmission.

2.2.1 Sound Speed Variation

The speed of sound is one of the most important acoustical parameters of the ocean. According to Newton's equation [25], the sound speed – a dynamic quantity - can be derived from certain static measurements on fluids. For many years, this method gave the most accurate values of sound speed in sea water over a wide range of pressure, temperature, and salinity.

$$c = (\rho\kappa)^{-1/2} \tag{2.1}$$

where c is the velocity of sound, ρ is the density of the ocean, and κ is the adiabatic compressibility. Since κ defined as

$$\kappa = \frac{1}{v}\frac{\partial v}{dp} \tag{2.2}$$

$$v = \frac{1}{\rho} \tag{2.3}$$

and v is the specific volume, Eq. (2.1) can be rewritten as:

$$c = v\left(\frac{\partial p}{\partial v}\gamma\right)^{1/2} \tag{2.4}$$

where the ratio of specific heats (γ) is the conversion factor from the measured isothermal quantity to the adiabatic values.

From experimental results and theoretical considerations, a number of equations for sound speed have been proposed. A typical example of an empirical sound speed equation is shown in Eq. (2.5) [2, 26]:

$$c = 1449 + 4.6T - 0.055T^2 + 0.0003T^3 + (1.39 - 0.012T)(S - 35) + 0.017z \qquad (2.5)$$

where c is the sound of speed in m/sec, T is the temperature in degree Celsius, S is the salinity in parts per thousand, and z is the depth in meters. Because the speed of sound increases with increasing water temperature, salinity, and pressure, it changes significantly with season, time of day, depth, and geographical position.

The characteristic of sound speed variation with depth, namely, the sound speed profile, can be seen in Figures 2.3 and 2.4 (from [25] and [2], respectively). The examples shown are typical in the South Pacific Ocean and the North Atlantic Ocean, respectively.

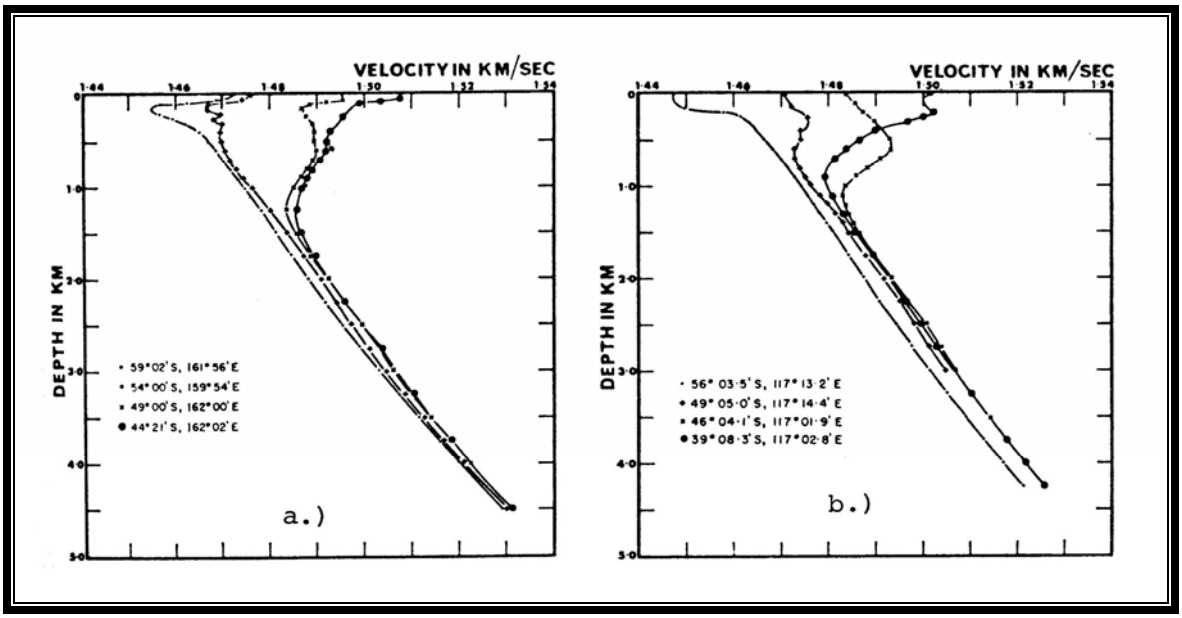

Figure 2.3 – Sound speed profile in different latitudes along the South Pacific Ocean [25]
a) 160°E, b) 117°E

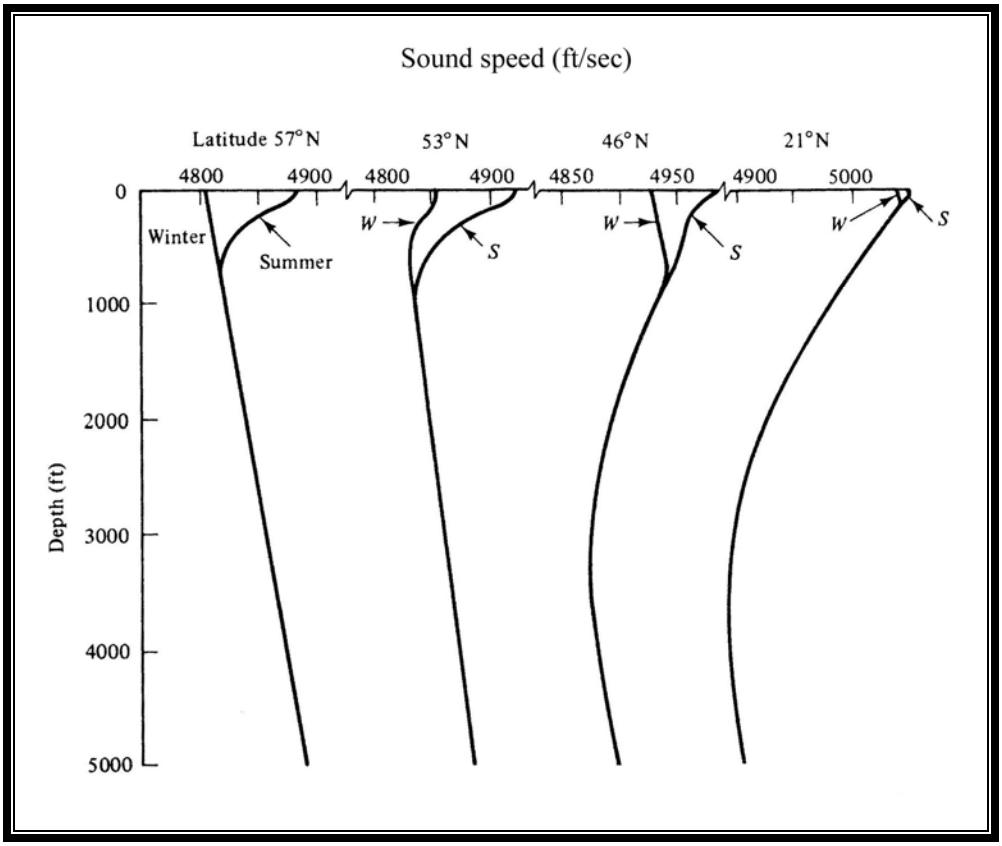

Figure 2.4 – Sound speed profile variation with latitude in the North Atlantic Ocean [2]

2.2.2 Absorption of Sound in the Ocean

Absorption loss involves the conversion portion of the energy of sound wave into heat and results from heating up of the medium in which it occurs. The measurements of the absorption coefficient (α) typically expressed in units of decibels per Kilometer, span the frequency range from 20 Hz to 60 KHz. The best known absorption loss coefficient is probably that developed by Thorp in 1967 and is valid at frequencies below 50 KHz [30]:

$$\alpha = 1.0936\left[\frac{0.1f^2}{1+f^2} + \frac{40f^2}{4100+f^2}\right] \tag{2.6}$$

where α is the absorption coefficient in dB/Km and f is the frequency in KHz.

Some of the causes of absorption loss are well known. In fresh water, the measured absorption losses are adequately explained by consideration of viscosity effects. In sea water, the measured absorption losses below 100 KHz are considerably anticipated from viscosity effects also. Magnesium sulfate ion has been identified also as a significant contributor to absorption loss. A similar effect also occurs at frequencies below 5 KHz with the boric acid ion. Figure 2.5 below gives the absorption loss as a function of frequency in the ocean [2].

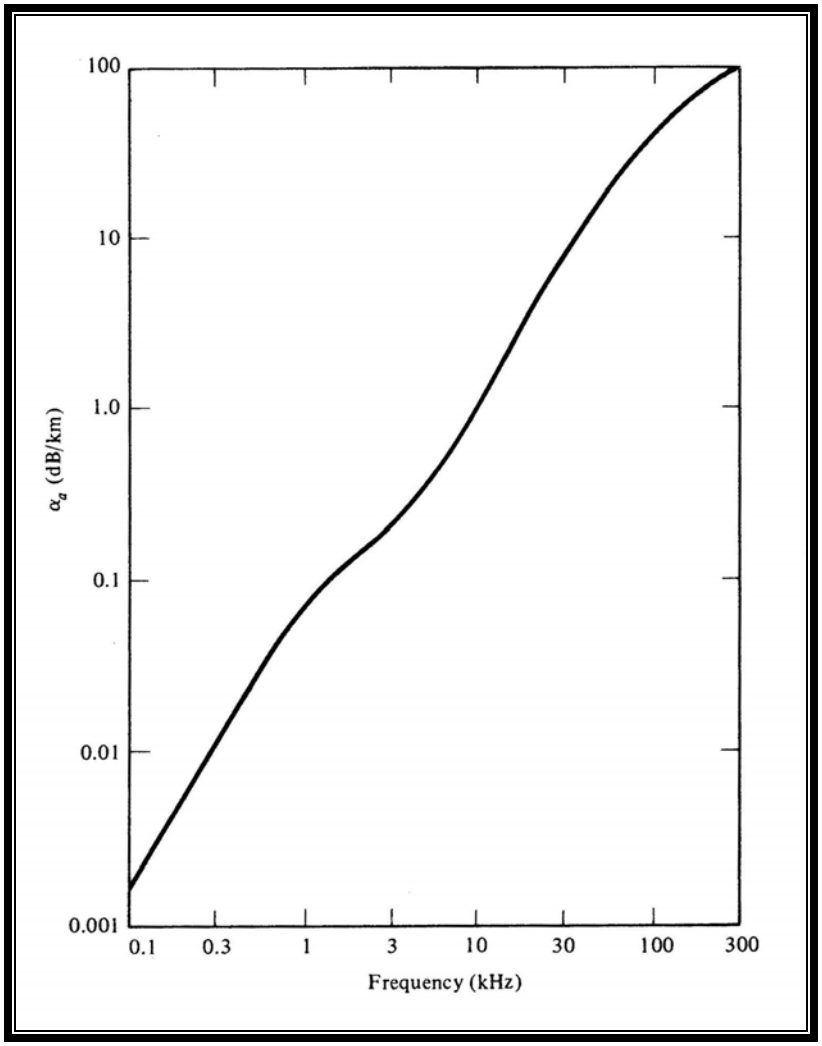

Figure 2.5 – Absorption loss in the ocean [2]

The absorption loss increases with both frequency and range. It is the primary factor determining the maximum usable frequency, and therefore the available bandwidth. Since absorption loss increases with frequency, high frequencies are practical only for short ranges.

2.3 REVERBERATION

Reverberation due to multipath is the most challenging aspect in the underwater acoustic channel. The mechanisms of multipath formation in the ocean are different in deep and shallow water. Reverberation also depends on the frequency and range of transmission. Two fundamental mechanisms for multipath formation are reflection at the boundaries (bottom, surface, and any objects in the water) and ray bending.

2.3.1 Acoustic Loss at the Ocean Surface and Bottom

The acoustic loss at the ocean surface is primarily caused by the reflection of acoustic rays because of the large impedance mismatch at the boundary of air and water and the non-planar shape of the surface. If the surface is not perfectly smooth, the acoustic rays are reflected in a random manner. As the interface becomes very rough, diffuse reflection occurs, resulting in large acoustic energy losses. The roughness of a surface can be defined by

$$R = 2kh\sin\theta \tag{2.7}$$

where R is the roughness coefficient, k is the acoustic wave number ($k=2\pi/\lambda$) with λ the wavelength, h is the height of the roughness feature, and θ is the grazing angle. When $R<<1$ the surface is empirically considered smooth; when $R>>1$, the surface is considered rough [25]. With this criterion, the expression for surface reflection loss (α_s in dB) can be

derived as a function of the product of the average trough-to-crest wave height (H in ft) and acoustic frequency (f in KHz) in Eq. (2.8) with the assumption of a small grazing angle [2].

$$\alpha_s = -10\log_{10}[1 - 0.0234(fH)^{3/2}] \tag{2.8}$$

Figure 2.6, from [2], shows an example of the graphical representation of acoustic loss per surface reflection, or "bounce."

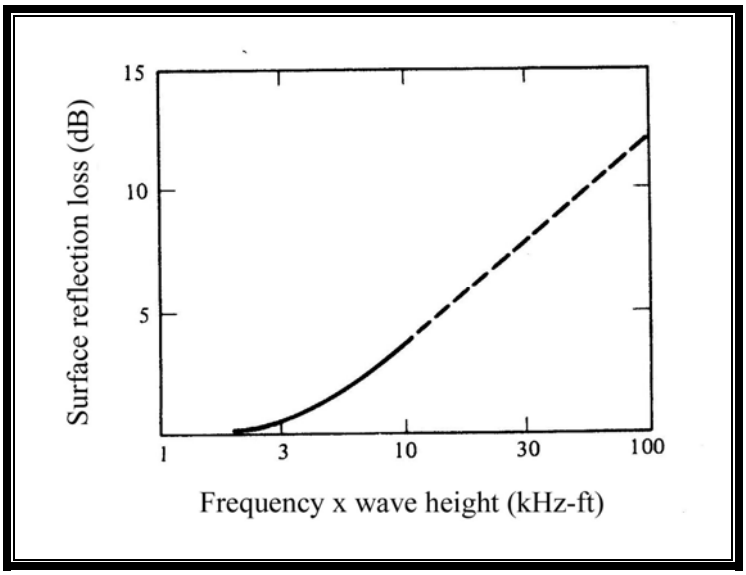

Figure 2.6 – Sea surface reflection loss at low grazing angle [2]

The computation of the reflection loss at the ocean bottom is more complex than that at the ocean surface, even when the bottom is perfectly flat. Portions of the acoustic energy may be reflected directly from the bottom surface; portions of it may be transmitted into the layers of sediment on the bottom floor and be absorbed by the sediments, or may be refracted back to the ocean. The resulting reflection coefficient involves both a loss in amplitude and a phase change relative to the incident wave. The loss of acoustic intensity encountered at the ocean bottom is harder to predict than the loss at the ocean surface.

The bottom ocean reflection loss (α_b in dB) is defined in Eq. (2.9) where Z_2/Z_1 is the ratio of characteristic impedances of bottom sediment and water, θ_i is the grazing angle relative to the ocean floor, and θ_t is the angle of the transmitted or refracted wave in the ocean floor [2]:

$$\alpha_b = -20\log_{10}\left[\frac{(Z_2/Z_1)\sin\theta_i - \sin\theta_t}{(Z_2/Z_1)\sin\theta_i + \sin\theta_t}\right] \tag{2.9}$$

Because sound speed in water is less than that in the ocean floor, the θ_i should be less than the critical grazing angle (θ_c) for total reflection and the reflection loss should theoretically be zero.

$$\theta_c = \arccos\left(\frac{c_1}{c_2}\right) \tag{2.10}$$

where c_1/c_2 is the ratio of sound speeds in water and the ocean floor

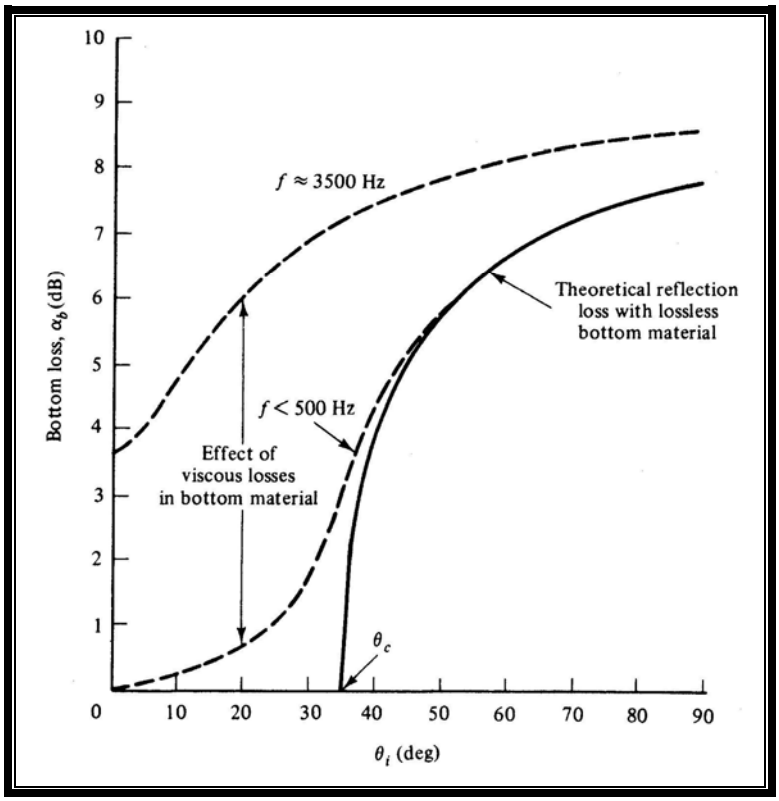

Figure 2.7 – Sea bottom reflection loss for a smooth, coarse sandy bottom [2]

Figure 2.7 shows an example of the bottom reflection loss for a smooth, coarse sandy bottom. As we can see, the reflection loss increases with increasing frequency (dashed curves), even at low grazing angle the reflection loss is not zero.

According to U.S. Naval Fleet Numerical Weather Center (FNWC) [2], there are nine bottom classes, starting with a low loss sandy bottom.

2.3.2 Scattering

There are several significant causes of scattering that result in reverberation. The main contributors in the body of ocean are probably the biological sources such as fish, plankton, and other biological sources. These sources of reverberation are called volume reverberation. The level of the volume-scattering strength depends on the seasonal standing crop of scatterers, which may exhibit inter-annual variability. For simplicity, often times the volume reverberation is assumed uniformly distributed over the region of interest even though in practice this may not be so. Another type of scattering reverberation is the surface reverberation which occurs because of the inhomogeneities and roughness of the top and bottom surfaces of the ocean.

The fundamental ratio upon which reverberation depends is called the scattering strength. Scattering strength is defined as the target strength with respect to a point target [2].

$$S_v = 10\log_{10}\left(\frac{I_r/v}{I_i}\right) = S_s \tag{2.11}$$

where S_v and S_s are the volume and surface scattering strengths, respectively, I_i is the intensity of the incident signal, I_r is the intensity of the reflected signal and v is the unit volume.

Modeling scattering theory is very complex due to its dependency on the season and location. Complete details of the physical and mathematical models of reverberation due to scattering strength can be found in [30], and will not be discussed further here.

2.4 SPREADING

Relative motion of source, receiver, and scattering objects change the frequency of transmitted signals. This change can be in time and/or in frequency. Change in time is called time delay and change in frequency is called the Doppler spread. When the signal is both time delayed and Doppler spread, we have a doubly spread channel. Underwater communication channels are generally doubly spread. Both time delay and Doppler spreading are important factors in the acoustic communication channel, and any design must recognize each.

The impact of the travel time and Doppler spreads for a signal are often classified into two types: underspread and overspread. If a channel has a bandwidth B and has a fading time constant on the order of $1/B$, then when a signal if a symbol duration T is transmitted, there are approximately BT uncorrelated samples of its complex envelope. When BT is much less than unity, the channel is said to be underspread in Doppler. In this case, the effects of Doppler fading can be ignored. When BT is larger than unity, then the channel is said to be overspread.

As mentioned in chapter one, the main constraints on underwater communications are the available bandwidth, rate of change of the channel, and available power. The tradeoff for optimal communication systems is often between bit rate, reliability, and range. To obtain a longer signal transmission range, the bit rate may have to be decreased. The effects of delay and Doppler spread are complementary in the sense that

as the bit rate on the channel increases, the delay spread spans over more symbols, and this gives more inter-symbol interference (ISI). When the bit rate decreases, the channel variation from one symbol to the next increases. This means that a given Doppler spread requires better tracking bandwidth at the receiver.

There are many ways to characterize underwater communication channel with the time delay and Doppler spread. [10, 11] use the delay-Doppler-spread function $U(\tau,\upsilon)$ to represent time and frequency dispersive channels.

$$y(t) = \iint z(t-\tau)U(\tau,\upsilon)\exp[j2\pi\upsilon]d\tau d\upsilon \tag{2.12}$$

where $y(t)$ is the channel output, $z(t)$ is the channel input, υ is the Doppler shift, and τ is the delay. The quantity $U(\tau,\upsilon)\, d\tau\, d\upsilon$ is the contribution to the output $y(t)$ from a scatterer at delay τ and Doppler υ.

2.5 STATISTICAL CHANNEL MODEL

In signal detection theory, channel modeling is important because of the need to mathematically formulate the physical conditions which play important roles. Due to the random nature of the underwater media, statistical manipulations of the mathematical underwater channel models are necessary. Even after simplification, the underwater acoustic channels are still particularly difficult to model statistically because of the nonhomogeneous and nonstationary character of these channels.

In this research, two widely used distributions – Gaussian and Rayleigh – are employed to model the underwater communication channel. Many researchers use the Additive White Gaussian Noise (AWGN) to model the ambient noise in underwater channels such as in [5, 8, 10, 11, 28]. In some cases, authors also used the Gaussian

distribution to model the phase shift or the time delay [5]. However, [6] believes that the delay and the phase shift are stable enough that they can be considered to be deterministic; we follow this approach. However, due to fading multipath characteristics of the underwater channel, many researches have preferred to model the underwater channel using the non-Gaussian models. Some, as we do, believe that the channel amplitude response can be modeled by a Rayleigh distribution [5, 33] although there are still disagreements [7]. This is the reason that underwater channel modeling is still a current and active research topic.

2.5.1 Additive White Gaussian Noise (AWGN) Channel

The fundamental communication channel, the Additive White Gaussian Noise channel (AWGN), is chosen as the first channel model for our simulations. There are three facts about the Gaussian density which contribute to its wide use and success in representing most communication channel models [31]. First, many physical processes are indeed Gaussian, primarily those having to do with the basic thermal noise in the systems. Second, the central limit theorem states essentially that any process which is the result of combination of elementary random processes acting in concert will tent to be Gaussian. Finally, linear systems preserve Gaussianity, in that the output of a linear stationary system, excited by stationary Gaussian process, is itself Gaussian; therefore, the simplicity and convenient characteristics of Normally distributed variables propagate along the channels or systems.

For our first model, then, the channel is assumed to be linear and stationary, with ambient noise represented by the Additive White Gaussian Noise.

Let's say that the signal *s(t)* is transmitted through the underwater channel. The received signal *r(t)* can be modeled as follow:

$$r(t) = A_r[s(t) + n(t)] \tag{2.13}$$

where A_r is some scaling constant, *n(t)* is the zero-mean stationary Gaussian random process with probability density function (PDF) at time *t* of:

$$f_g(n) = \frac{1}{\sigma_g \sqrt{2\pi}} \exp\left[-\frac{(n - < n >)^2}{2\sigma_g^2} \right] \tag{2.14}$$

where σ_g^2 is the variance and $<n>$ is the mean noise, independent of time. For a white Gaussian noise, the mean is zero.

According to the Channon-Hartley theorem, the channel capacity $\hat{C}_g$ of a white bandlimited Gaussian channel can be expressed as [32]:

$$\hat{C}_g = W \log_2(1 + \gamma) \text{ b/s} \tag{2.15}$$

where *W* is the channel bandwidth and γ is the carrier to noise ratio

$$\gamma = \frac{C}{N} \tag{2.16}$$

with *C* the signal power and *N* is the Gaussian noise power. This theorem indicates that with a specific information rate, the signal power and bandwidth are inversely related to each other. It also indicates that a noiseless Gaussian channel has an infinite capacity when γ or *B* approach infinity.

For the Additive White Gaussian Noise (AWGN) channel, we define our signal-to-noise ratio as:

$$SNR(dB) = 10 \log_{10} \frac{E_s}{E_n} \tag{2.17}$$

with E_s as the signal energy in one symbol *s(t)* and E_n is the double sided power of the white Gaussian noise process, given as:

$$E_n = 2W\sigma_g^{\,2} \tag{2.18}$$

where W is defined as the channel bandwidth and σ_g^2 is the variance of the AWGN.

2.5.2 Rayleigh Fading Channel

In the previous section, we assumed the received signal *r(t)* with a constant amplitude scaling or attenuation A_r (normalized to 1) for both the signal and the noise. In this section, the amplitude scaling factor A_r will be considered to be a random variable where random multiplicative noise is present in the channel. Here the Rayleigh distribution will be used to model the amplitude attenuation.

Again, the signal *s(t)* is transmitted through the underwater channel. For convenience, the model of the received signal *r(t)* in Eq. (2.13) is written again as:

$$r(t) = A_r(t)[s(t) + n(t)]$$

where *n(t)* is the zero-mean stationary Gaussian random process and $A_r(t)$ is the Rayleigh fading random process with probability density function (PDF) at time *t* of:

$$f_r(n) = \begin{cases} \dfrac{n}{\sigma_r^{\,2}} \exp\left[\dfrac{-n^2}{2\sigma^2}\right] & n > 0 \\ 0 & n \le 0 \end{cases} \tag{2.19}$$

The mean and the variance of the Rayleigh distribution are as follows:

$$\mu_r = \sigma\sqrt{\frac{\pi}{2}} \tag{2. 20}$$

$$\sigma_r^2 = \left(2 - \frac{\pi}{2}\right) \tag{2. 21}$$

The average channel capacity $\left\langle \hat{C}_r \right\rangle$ in a Rayleigh fading environment can be expressed as in Eq. (2.22) [32]. $\left\langle \hat{C}_r \right\rangle$ has to be calculated in an average sense because the carrier to noise ratio of Rayleigh fading varies with time.

$$\left\langle \hat{C}_r \right\rangle = \frac{B}{\ln 2} e^{-1/\Gamma} \left[-E + \ln\Gamma + \frac{1}{\Gamma} - \frac{1}{(2\cdot 2!)\Gamma^2} + \frac{1}{(3\cdot 3!)\Gamma^3} - \frac{1}{(4\cdot 4!)\Gamma^4} + \ldots \right] \tag{2. 22}$$

where B is the channel bandwidth, Γ is the average power of the carrier-to-noise- ratio γ, and E is the Euler constant ($E = 0.5772157$).

$$\Gamma = \langle \gamma \rangle = \frac{\langle C \rangle}{N} \tag{2. 23}$$

again, C is the signal power and N is the Rayleigh noise power.

The channel capacity in a Rayleigh fading channel is always lower than that in a Gaussian noise channel. As shown in Figure 2.8, the channel capacity of a Rayleigh fading channel is reduced by 32% from the Gaussian channel at $\Gamma = 10$ dB, and reduced only by 11% at $\Gamma = 25$ dB.

We define our signal-to-noise ratio as:

$$SNR(dB) = 10\log_{10}\frac{E_{Rs}}{E_n} \tag{2.24}$$

where E_{Rs} is the average energy in one faded symbol $A(t)s(t)$:

$$E_{Rs} = E\left\{\left[A(t)S(t)\right]^2\right\} \tag{2.25}$$

with $A(t)$ the Rayleigh amplitude. The SNR of (2.24) can therefore be rewritten as

$$SNR(dB) = 10\log_{10}\frac{a_r^2 E_s}{E_n} \tag{2.26}$$

a_r is the Rayleigh power parameter and E_n is again the double sided power of the white Gaussian noise defined in Eq. (2.18).

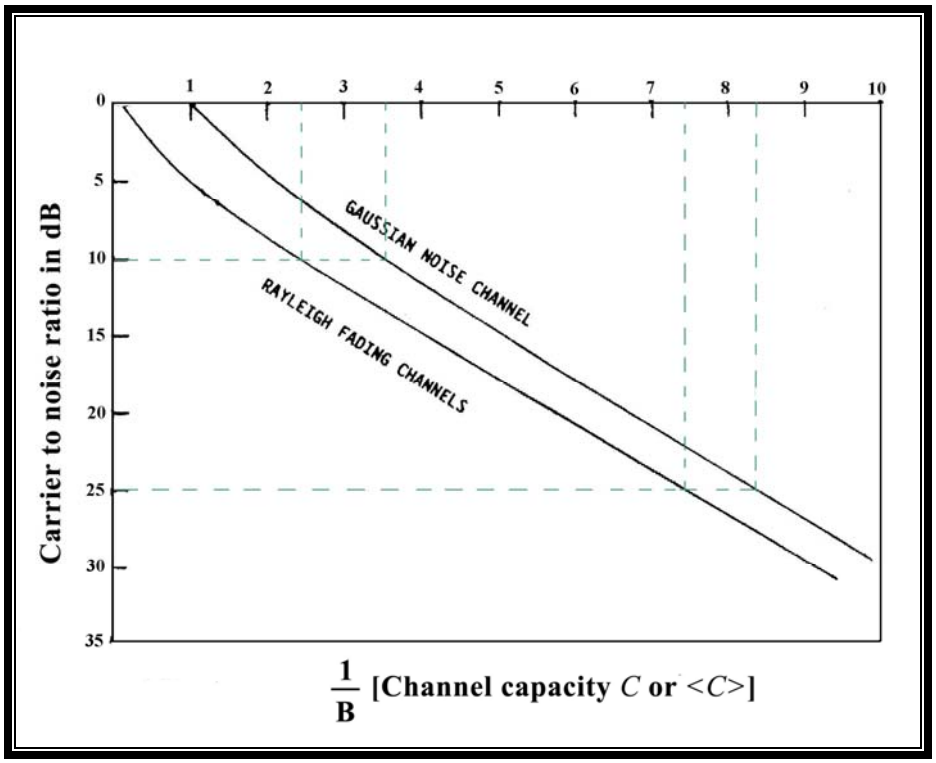

Figure 2.8 – Channel capacity in Gaussian noise and Rayleigh fading channels [32]

3. CHIRP-SLOPE-KEYING MODULATION

The term “chirp” comes from the bird chirp or cricket sounds – a short pulse, high-pitched sound. This pulse is called a “chirped” pulse. The name “chirp” was coined by the Bell Telephone Laboratories. Scientifically, the term “chirp” means a wave whose instantaneous frequency varies over time. Chirps come in many frequency sweep forms: linear up-, linear down-, quadratic-, logarithmic-chirp, etc. Figure 3.1 shows spectrogram examples of the linear-up-chirp and quadratic-chirp signals.

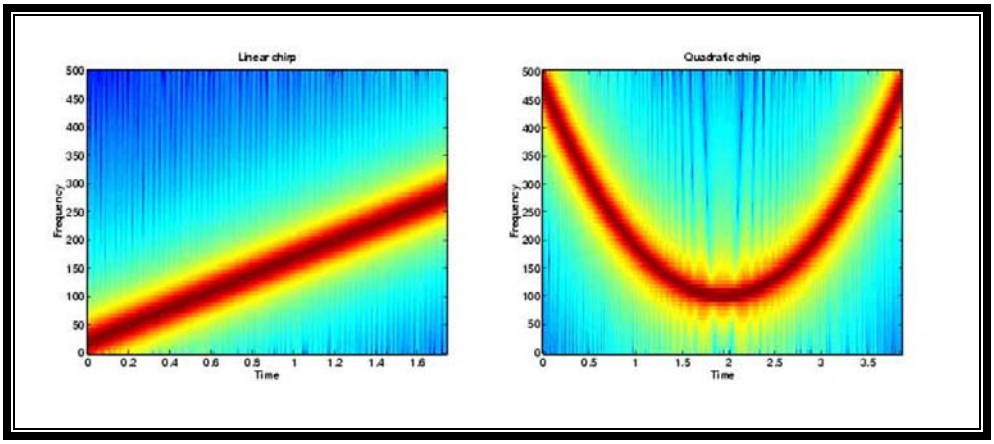

Figure 3.1 – Spectrograms of linear up-chirp and quadratic-chirp

Linear chirp signals – mostly known as linear frequency modulation (linear-FM) signals in radar and sonar – have been used in radar technology since the mid-1940s. Chirp pulses are used in radar in an attempt to enhance range resolution with pulses much longer than would ordinarily be employed in a high-range resolution radar [29]. Now chirp signals are employed in other systems such as in sonar systems and communication systems.

Because of the wide bandwidth characteristic of chirp signals, chirp modulation is classified as a spread spectrum technique. The spreading of bandwidth gives chirp modulation advantages over other modulation schemes (e.g. amplitude-shift-keying (ASK), frequency-shift-keying (FSK), phase-shift-keying (PSK), etc.). These advantages include resistance to multipath, decorrelation of impulsive type noise, resistance to jamming interference, and immunity to frequency selective fading [12].

3.1 GENERAL CHIRP SIGNAL MODEL

The general expression of the transmitted signal *s(t)* is given by:

$$s(t) = d(t)c(t) \qquad 0 \le t < T \tag{3.1}$$

where *d(t)* is the envelope of the chirp signal, *c(t)* is the chirp signal, and *T* is the symbol period. At the receiver, the general expression of the received signal can be written as:

$$r(t) = A_r(t)[s(t) + n(t)] \tag{3.2}$$

where *n(t)* is the additive noise and $A_r(t)$ is amplitude gain. For easier analysis, $A_r(t)$ is set to be 1. However, $A_r(t)$ can easily be randomized with Rayleigh distribution.

Now, let's observe the design of a chirp signal

$$c(t) = \cos(\Theta(t)) \tag{3.3}$$

where $\Theta(t)$ is the phase. The instantaneous frequency is defined as

$$f(t) = \frac{1}{2\pi}\frac{d\Theta}{dt} \tag{3.4}$$

and the chirp rate $\mu(t)$ is defined by the derivative of the instantaneous frequency

$$\mu(t) = \frac{df(t)}{dt} = \frac{1}{2\pi}\frac{d^2\Theta}{dt^2} \tag{3.5}$$

The waveform in which $\mu(t) > 0$ is called an up-chirp, and the waveform in which $\mu(t) < 0$ is called a down-chirp. For linear chirps, $\mu(t)$ has to be a constant, and hence $f(t)$ is a linear function of t and $\Theta(t)$ is a quadratic function of t. Thus, a linear chirp signal can be rewritten as follows:

$$c(t) = \cos\left(2\pi f_0 t + \pi\mu t^2 + \theta_0\right) \tag{3.6}$$

where f_0 and θ_0 are the initial frequency and phase, respectively, and μ is the chirp rate in hertz per time period T. The chirp rate μ is defined in Eq. (3.7) where f_{max} and f_{min} are the maximum and minimum frequencies of a chirp signal for the duration $\Delta t = t_{max} - t_{min}$.

$$\mu = \frac{f_{\max} - f_{\min}}{t_{\max} - t_{\min}} \tag{3.7}$$

Then, the bandwidth of B is:

$$B = f_{\max} - f_{\min} \tag{3.8}$$

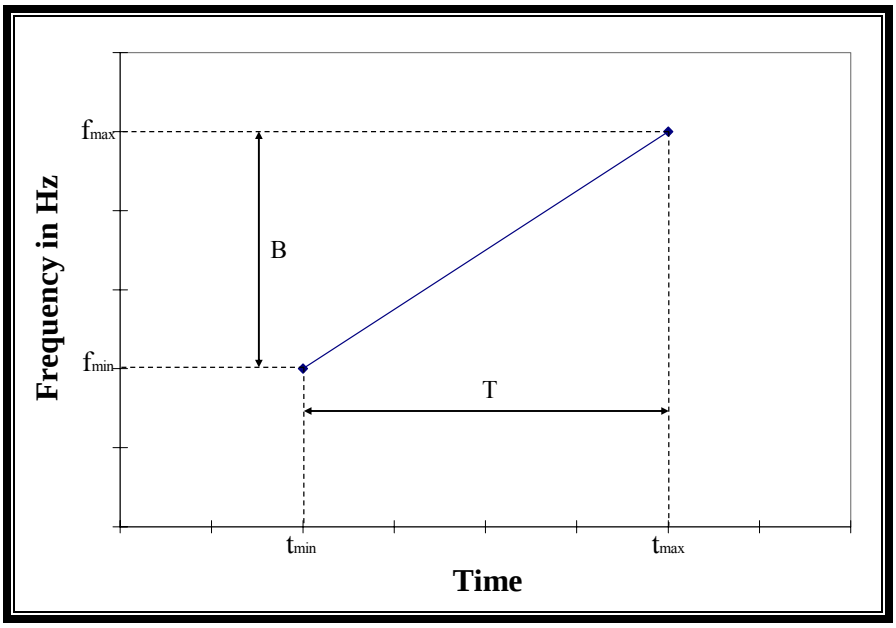

Figure 3.2 – Frequency vs. Time Plot for linear-up-chirp

From this point on, all mention of chirp signals will refer to the linear-chirp signal.

3.2 LINEAR CHIRP RECEIVER STRUCTURES

As we can see in Figure 3.2, the digital information to be transmitted using CSK is contained in the slope of the frequency not in the phase, or amplitude, or frequency as is the case in PSK, ASK, and FSK, respectively. This section briefly discusses several receiver structures that could be used to detect the linear frequency slope of the chirp signal. The only structure we actually simulated is the integrate-and-dump detector, but we expect some other receivers to perform better when phase delays, time delays, and Doppler are present.

The *integrate-and-dump detector* is a simple and sub-optimal implementation of the matched filter detector. This detector acts as a lowpass predetection filter. It integrates the received signal over a period interval and then thresholds the result to determine the bit data (a 0 or a 1). The integrate-and-dump detector has been widely used to demodulate the standard binary phase shift keying (BPSK). Figure 3.3 shows the receiver structure for an integrate-and-dump detector with BPSK signal.

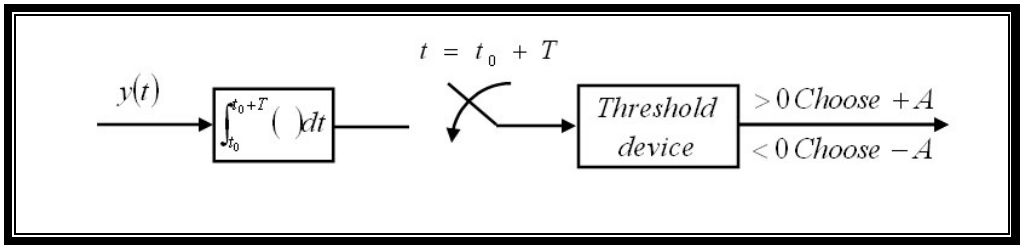

Figure 3.3 – Integrate-and-dump receiver structure

A *matched filter* may also be used for demodulation. The matched filter measures the similarity between the received signal and an impulse response, *h(t)*, at the receiver. The purpose of the matched filter is to maximize the signal-to-noise ratio (SNR) and to minimize the probability of error. The receiver structure for a matched filter is shown in

Figure 3.4. After the sampler, a threshold device will compare the difference of the output, not shown in the figure.

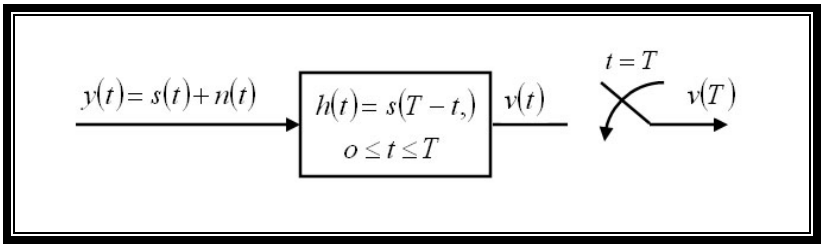

Figure 3.4 – Matched filter receiver structure

An equivalent detection operation to the matched filter detector is the *correlation detection*. It utilizes a multiplier-integrator cascade. The proposed detection for our CSK employs the correlation detector. It is basically identical to standard BPSK receiver already in operation which could be directly used by changing only the signal into the receiver's multiplier. The correlator receiver structure is shown in Figure 3.5. Similarly to Figure 3.3, after the sampler, the output will go through a threshold device.

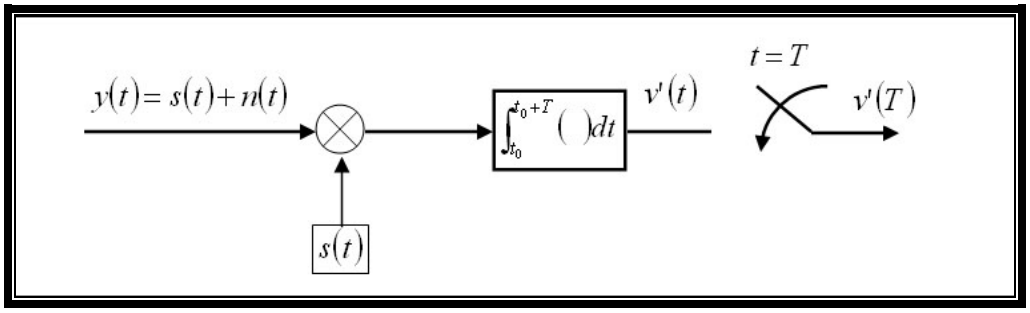

Figure 3.5 – Correlator receiver structure

Another possible detector structure is one that determines the slope of the frequency sweep by using a line detection method such as the Hough Transform. Hough Transform is a technique for line detection, and has been widely used in image processing. The same technique can be used to detect the frequency slope of the chirp signal. Hough Transform can easily distinguish between the up- and down-chirp even when the signal is highly distorted. However, the operation of Hough Transform is much

harder to implement and slower than the integrate-and-dump receiver we implemented in our simulations.

3.3 CHIRP SLOPE KEYING MODULATION

This section discusses the proposed chirp slope keying modulation (CSK) system. The basic mathematical structure of the system will be presented.

A digital binary data are used to modulate the chirp signals. Binary describes a numbering scheme where there are only two possible values for each digit: a 0 and a 1. The 0 and 1 value are sometimes called "low/space/down" and "high/mark/up," respectively. These binary data are also referring to any digital encoded/decoded system in which there are also exactly two possible states: positive and non-positive. Again, the positive state is represented by a 1 and the non-positive state is represented by a 0. Each of these state digits is referred to as a bit.

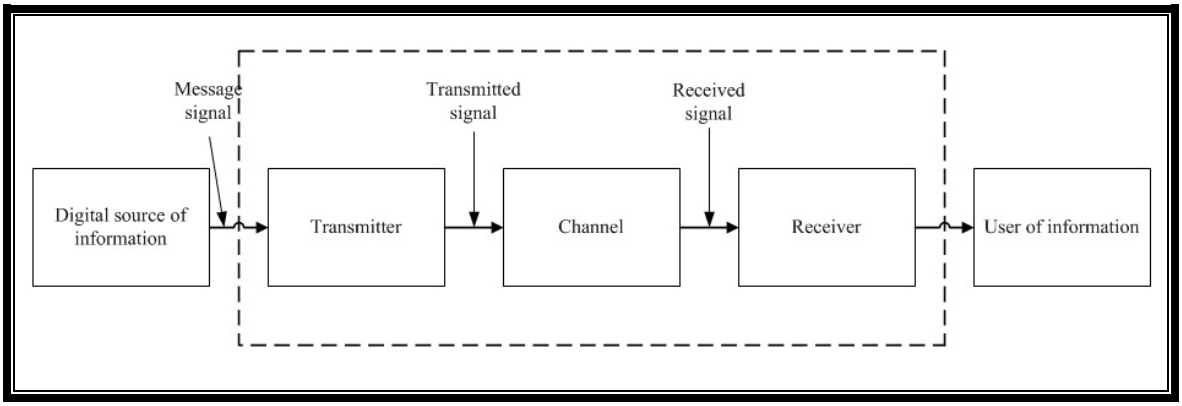

Figure 3.6 – Block diagram of a communication system

Figure 3.6 shows the general block diagram of any communication system. The system is divided into three parts: transmitter, channel, and receiver. The function of the transmitter is to convert the binary digital signal into a waveform (in our case it will be in the form of chirp signals) suitable for transmission over the channel. The function of the

receiver is to operate on the distorted or noisy received signal and deliver a reliable estimate of the original binary digital signal to a user at the output of the system.

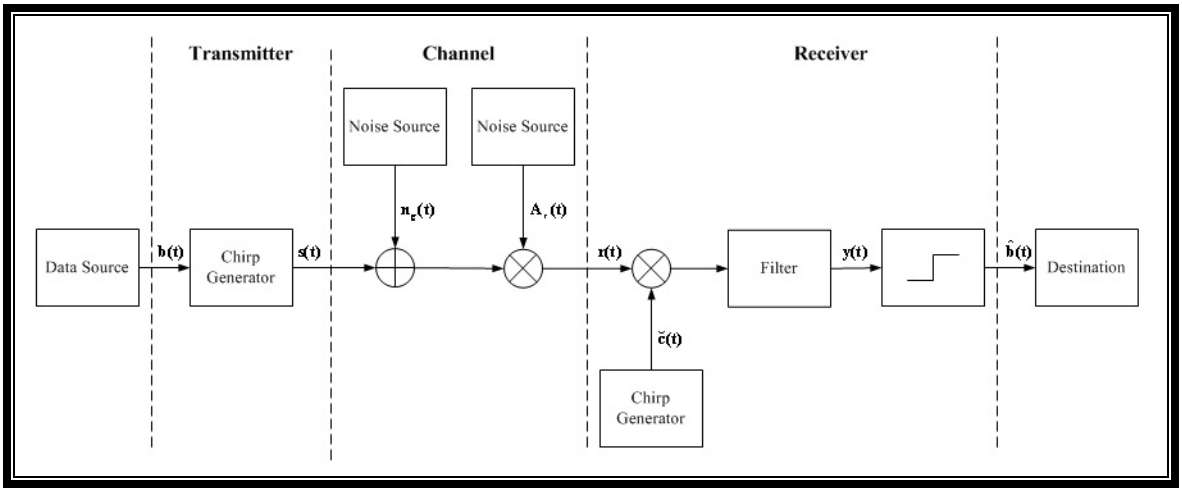

Figure 3.7 – Model of new chirp slope keying modulation system

Figure 3.7 shows a more detailed version of the block diagram of a communication system employed in this research. The data source generates a binary data sequence *b(t)* to be sent through an underwater channel. At the transmitter, the binary data sequence $b_i(t)$ is directly mapped to its chirp signal sequence $c_i(t)$. Binary data "1" is modulated with an up-chirp signal and binary data "0" is modulated with a down-chirp signal. The transmitted signal can be written as follows:

$$s(t) = c(b,t) \tag{3.9}$$

where *s(t)* is the modulated binary data. *c(b,t)* is the chirp signal, which is a function of the binary data from the data source and of time. Expanding Eq. (3.9) with Eq. (3.6), *s(t)* can be rewritten as follows:

$$s_b(t) = \cos\left(2\pi f_0 t + \pi\mu(2b-1)t^2 + \theta_0\right), \qquad b = 0,1 \tag{3.10}$$

where μ is the chirp rate/slope of the frequencies sweep, as given in Eq. (3.7). For every binary data $b = 1$, the chirp signal is made of an increasing frequency sweep; and for every binary data $b = 0$, the chirp signal is made of a decreasing frequency sweep.

Then the signal $s_b(t)$ is transmitted over a noisy underwater channel. In this research, the noisy channel includes the Additive White Gaussian Noise (AWGN) ($n_g(t)$) and Rayleigh amplitude fading ($A_r(t)$).

$$r(t) = A_r(t)\left[s(t) + n_g(t)\right] \tag{3.11}$$

For detection of the data sequence at the receiver, the signal is demodulated by multiplying the received signal with another up-chirp, *č(t)*. The multiplication result is then subsequently filtered by integrating over one symbol period. By using a threshold, the demodulated received signal *y(t)* is estimated to its original data sequence, $\hat{b}(t)$. For simplicity, the received signal *r(t)* is assumed to be synchronized with *č(t)*.

3.3.1 Mathematical Model

Below is the prototype of the mathematical algorithm for the proposed underwater wireless communication system in a noiseless channel. Let's define the parameters once more:

Binary data $b = 1 \coloneqq s_u$ (up-chirp)

Binary data $b = 0 \coloneqq s_d$ (down-chirp)

$$s_u(t) = \cos\left(2\pi f_{\min} t + \pi\mu t^2 + \theta_u\right) \tag{3.12a}$$

$$s_d(t) = \cos\left(2\pi f_{\max} t - \pi\mu t^2 + \theta_d\right) \tag{3.12b}$$

or, equivalently,

$$s_u(t) = \cos\left(2\pi f_{\min} t + \pi t^2 + \theta_u\right) \tag{3. 13a}$$

$$s_d(t) = \cos\left(2\pi f_{\max} t - \pi t^2 + \theta_d\right) \tag{3.13b}$$

f_{max} and f_{min} are the initial frequencies for the up- and down-chirp signals, respectively, μ is the slope or the chirp rate. Here, the magnitude of the slope for both

chirp signals is the same respectively, which implies both have the same bandwidth. f_{max} and f_{min} will also make sure that both chirp signals consist of the same frequencies (please refer to Figure 3.2). θ_u and θ_d are the initial phase and by initializing them to zero, the chirp signals become:

$$s_u(t) = \cos\left(2\pi f_{\min} t + \pi \mu t^2\right) \tag{3.14a}$$

$$s_d(t) = \cos\left(2\pi f_{\max} t - \pi \mu t^2\right) \tag{3.14b}$$

or, equivalently,

$$s_u(t) = \cos\left(2\pi f_{\min} t + \pi t^2\right) \tag{3.15a}$$

$$s_d(t) = \cos\left(2\pi f_{\max} t - \pi t^2\right) \tag{3.15b}$$

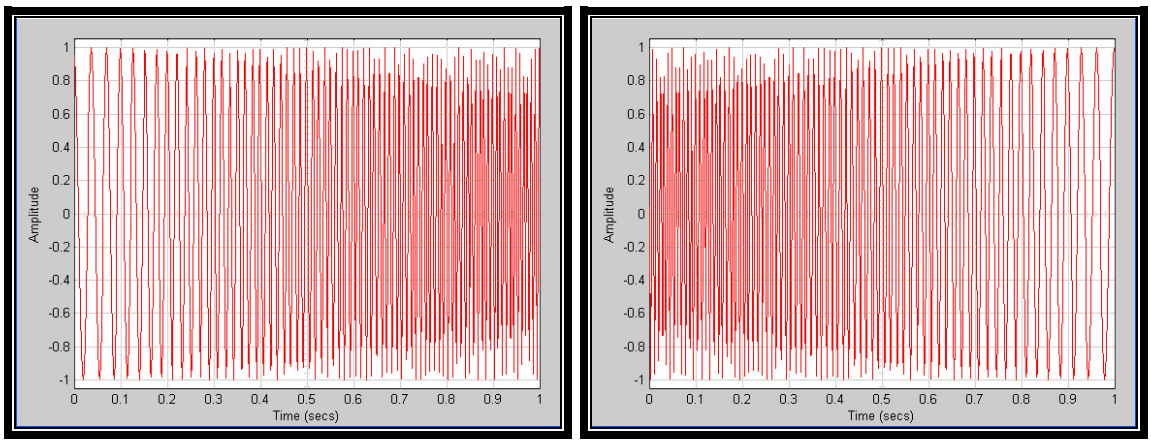

Figure 3.8 – Up-Chirp - s_u (left) and Down-Chirp - s_d (right)

Figure 3.8 shows the amplitude of the chirp signals from Eq. (3.14a) and Eq. (3.14b) with respect to time. The graph on the left and the right pertain to the up-chirp, s_u, and to the down-chirp, s_d, respectively. Figure 3.9 shows the power spectrum analysis. As we can see that both chirp signals have the same bandwidth and include the same frequencies, from 25 hertz up to 125 hertz. The ripples in the band center are caused by the Fresnel integrals [35].

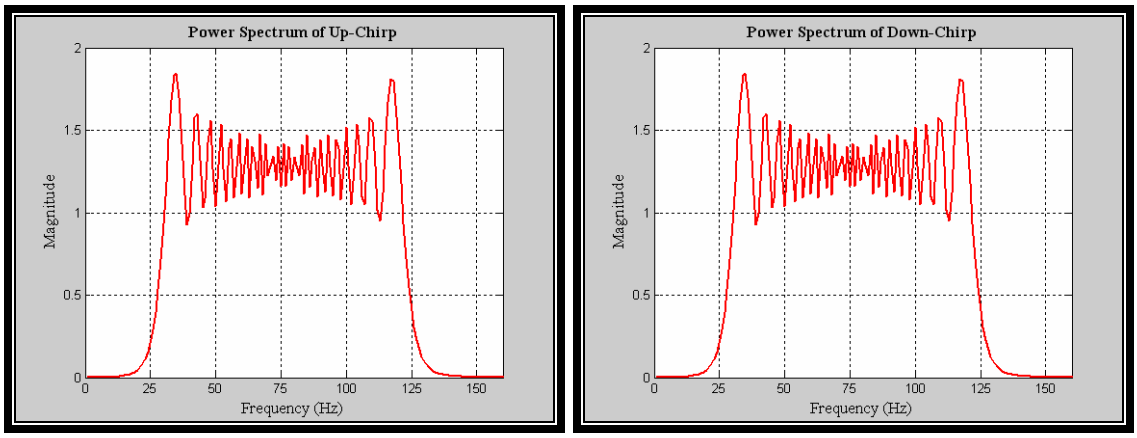

Figure 3.9 – Power Spectrum of Up-Chirp - s_u (left) and Down-Chirp - s_d (right)

At the receiver, the signal is demodulated by multiplying the received signal with another up-chirp, *č(t)*, before filtering.

$$\breve{c}(t) = \cos\left(2\pi f^* t + \pi\mu' t^2\right) \tag{3.16}$$

The multiplication gives:

$$y_u(t) = s_u(t)\breve{c}(t) = \cos\left(2\pi f_{\min} t + \pi\mu t^2\right)\cdot\cos\left(2\pi f^* t + \pi\mu' t^2\right) \tag{3.17a}$$

$$y_d(t) = s_d(t)\breve{c}(t) = \cos\left(2\pi f_{\max} t - \pi\mu t^2\right)\cdot\cos\left(2\pi f^* t + \pi\mu' t^2\right) \tag{3.17b}$$

or, equivalently,

$$y_u(t) = s_u(t)\breve{c}(t) = \cos\left(2\pi f_{\min} t + \pi t^2\right)\cdot\cos\left(2\pi f^* t + \pi\mu' t^2\right) \tag{3.18a}$$

$$y_d(t) = s_d(t)\breve{c}(t) = \cos\left(2\pi f_{\max} t - \pi t^2\right)\cdot\cos\left(2\pi f^* t + \pi\mu' t^2\right) \tag{3.18b}$$

If we let *č(t)* be exactly the same as the up-chirp s_u, then $\mu' = \mu$ and $f^* = f_{min}$. Then Eq. (3.17a) and Eq. (3.17b) become:

$$y_u(t) = \frac{1}{2} + \frac{1}{2}\left[\cos\left(4\pi f_{\min} t\right)\cos\left(2\pi\mu t^2\right) - \sin\left(4\pi f_{\min} t\right)\sin\left(2\pi\mu t^2\right)\right] \tag{3.19a}$$

$$y_d(t) = \frac{1}{2}\left[\cos\left(2\pi Bt\right)\cos\left(2\pi\mu t^2\right) + \sin\left(2\pi Bt\right)\sin\left(2\pi\mu t^2\right) + \cos\left(2\pi\left(f_{\max} + f_{\min}\right)t\right)\right] \tag{3.19b}$$

or, equivalently,

$$y_u(t) = \frac{1}{2} + \frac{1}{2}\left[\cos\left(4\pi f_{\min} t\right)\cos\left(2\pi t^2\right) - \sin\left(4\pi f_{\min} t\right)\sin\left(2\pi t^2\right)\right] \quad (3.\ 20a)$$

$$y_d(t) = \frac{1}{2}\left[\cos\left(2\pi B t\right)\cos\left(2\pi t^2\right) + \sin\left(2\pi B t\right)\sin\left(2\pi t^2\right) + \cos\left(2\pi\left(f_{\max} + f_{\min}\right)t\right)\right] \quad (3.20b)$$

where $B = f_{\max} - f_{\min}$.

The complete derivation of Eq. (3.19a) and Eq. (3.19b) can be found in Appendix 7.2.

Figure 3.10 shows the amplitude of *s(t)* after multiplying *č(t)*. We can see that the amplitude of $y_u(t)$ (the left graph) has been translated by ½, which is agreed with Eq. (3.19a). The graph on the right is referring to $y_d(t)$.

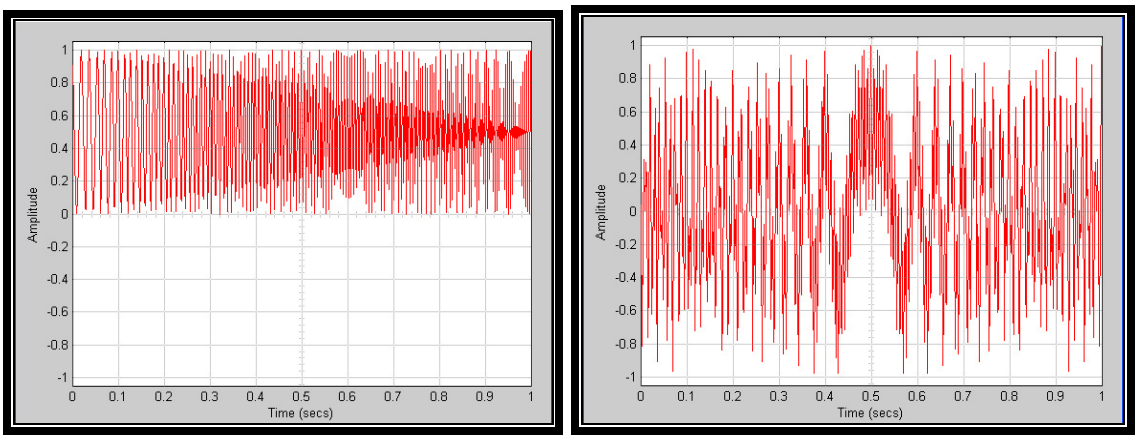

Figure 3.10 – $y_u(t)$ (left) $y_d(t)$ (right)

By applying a first order low pass filter (LPF) to the system with a cutoff frequency of much less than $2\pi B$ and $4\pi f_{min}$ ($f_c << 2\pi B$ & $4\pi f_{min}$), $y(t)$ leaves approximately with only the DC term:

$$y_u(t) = LPF\{y_u(t)\} \approx \frac{1}{2} \quad (3.21a)$$

$$y_d(t) = LPF\{y_d(t)\} \approx 0 \quad (3.21b)$$

By setting a threshold at the mid-point ¼, the binary sequence *b(t)* can be recovered, $\hat{b}(t)$. For all *y(t)* ≥ *1/4*, $\hat{b}(t)$ is the binary data "1"; and for all *y(t)* <*1/4*, $\hat{b}(t)$ is the binary data "0".

3.3.1.1. Original model

The mathematical model that is presented in section 3.3.1 (let's call it *Model B*) comes from the original model (let's call it *Model A*) that was developed in the year of 2001. The complete mathematical derivation can be found in Appendix 7.1. The difference between these two models is that in Model A, before filtering, the signal is multiplied by a pure cosine signal, *u(t)*. Mathematically, Model A shows better performance than that of Model B. We can easily filter out the frequencies present and be left with only the DC term by setting the cutoff frequency to much less than *2b* in *u(t)* – (equations are obtained from Appendix 7.1)

$$LPF\left[\mathrm{Re}\{S_U S_*\}\cos(bt)\right] = LPF\left[\frac{1}{2}+\frac{1}{2}\cos(2bt)\right] = \frac{1}{2}$$

$$LPF\left[\mathrm{Re}\{S_D S_*\}\cos(bt)\right] = LPF\left[\frac{1}{2}\cos(at^2)+\frac{1}{2}\cos(at^2+2bt)\right] \approx 0$$

In Model B, setting the cutoff frequency is not as easy because it depends on the minimum frequency presents in the system and on the bandwidth of the system (for easier analysis, Eq. (3.20a) and (3.20b) are listed again here). As we can see below, there are extra terms in the equations as compared to Model A.

$$y_u(t) = \frac{1}{2}+\frac{1}{2}\left[\cos(4\pi f_{\min} t)\cos(2\pi t^2)-\sin(4\pi f_{\min} t)\sin(2\pi t^2)\right]$$

$$y_d(t) = \frac{1}{2}\left[\cos(2\pi(f_{\max}-f_{\min})t)\cos(2\pi t^2)+\sin(2\pi(f_{\max}-f_{\min})t)\sin(2\pi t^2)+\cos(2\pi(f_{\max}+f_{\min})t)\right]$$

However, simulations show that Model B produces better BER results than Model A [36]; and this is due to the parameters of the chirp prime, $S_*(t)$, and the pure cosine, $u(t)$ (please refer to Appendix 7.1). In order for Model A to work, there are restrictions on the combinations of $S_*(t)$ and $u(t)$. In Model B, the only restriction is that the signal has to be multiplied with either the exact up- or down-chirp. Thus, the pure cosine signal has been omitted in all our simulations.

3.3.2 Power Calculation

Power is defined as:

$$P = \lim_{T\to\infty} \frac{1}{T} \int_{-T/2}^{T/2} s^2(t)dt \tag{3.22}$$

For a linear chirp signal, the power is then:

$$P = \lim_{T\to\infty} \frac{1}{T} \int_{-T/2}^{T/2} \cos^2\left(2\pi ft \pm \pi\mu t^2\right)dt \tag{3.23}$$

$$P = \frac{1}{2} + \frac{1}{2g}\left\{\cos\left(\frac{1}{2}\pi p^2\right)\cdot\left[C_f(p) - C_f(p+g)\right] + \sin\left(\frac{1}{2}\pi p^2\right)\cdot\left[S_f(p) - S_f(p+g)\right]\right\} \tag{3. 24}$$

where p and g define as:

$$p = \frac{2f}{\sqrt{\mu}} \tag{3. 25a}$$

$$g = 2T\sqrt{\mu} \tag{3.25b}$$

$$C_f(x) = \int_0^x \cos\left(\frac{1}{2}\pi t^2\right)dt \tag{3. 26a}$$

$$S_f(x) = \int_0^x \sin\left(\frac{1}{2}\pi t^2\right)dt \tag{3.26b}$$

$C_f(x)$ is the Fresnel Cosine and $S_f(x)$ is the Fresnel Sine.

With the assumption that the arguments of $C_f(x)$ and $S_f(x)$ in Eq. (3.24) are large numbers, the equations of $C_f(x)$ and $S_f(x)$ can be approximated to be approaching ½. The power of the linear chirp, then, can be approximated to be:

$$P = \frac{1}{2} + c \tag{3. 27}$$

where c is a small number.

3.3.3 Sampling Theorem

For our simulation, 100 Hz bandwidth chirp signals are considered with a linear frequency sweep of 25 Hz to 125 Hz for the up-chirp, $s_{u,}$ and a linear frequency sweep of 125 Hz to 25 Hz for the down-chirp, s_d. For simplicity, we also set the signaling interval to $T = 1$. These frequencies are chosen because of the time efficient in simulations, and should not be assumed to be the operational frequencies. However, simulations under higher frequencies and wider bandwidth will result in the same bit error rate. Discrete time signals in many applications are generated by sampling continuous time signals. In some cases, identical discrete time sequences may result from sampling more than one distinct continuous time function if the sampling rate is not chosen properly, or if the signal is not bandlimited. However, under certain conditions, it is possible to relate a unique continuous signal to a discrete time sequence and recover the exact continuous time signal from its sampled values (reconstruction).

Let's consider a signal $x(t)$ sampled uniformly at $t = nT_s$; generating its ideal instantaneous sampled waveform of the form:

$$x_\delta(t) = \sum_{n=-\infty}^{\infty} x(nT_s)\delta(t - nT_s) \tag{3.28}$$

where T_s is the sampling period. The reciprocal of T_s is called the sampling frequency $f_s = 1/T_s$.

To exactly recover the continuous time signal from its sampled value, one needs to follow the uniform sampling theorem from lowpass signals, which may be stated as follows [34]:

> *"If a signal x(t) contains no frequency components from frequencies above f = W hertz, then it is completely described by instantaneous sample values uniformly spaced in time with period $T_s < ½W$. The signal can be exactly reconstructed from the sampled waveform given by (3.18) by passing it through an ideal lowpass filter with bandwidth B, where $W < B < f_s - W$ with $f_s = T_s^{-1}$. The frequency 2W is referred to as the Nyquist frequency."*

For our chirp signals, the upper limit frequency is f_{max} = 125 Hz and the lower limit frequency is f_{min} = 25 Hz. Therefore, the Nyquist frequency is $f_s = 2f_{max}$ = 250 Hz.

Since chirp signals have a bandpass spectra with the upper limit frequency f_{max}, which is usually much larger than the single sided bandwidth, it is possible to naturally sample at rates less than $f_s < 2f_{max}$. The uniform sampling theorem for bandpass spectra gives the conditions for which this is possible, as follows [34]:

> *"If a signal has a spectrum of bandwidth W hertz and upper frequency limit f_H, then a rate f_s at which the signal can be sampled is $2f_H/m$ where m is the largest integer not exceeding f_H/W. All higher sampling rates are not necessary usable unless they exceed $2f_H$."*

In the definition above, f_H is the f_{max}. According to the uniform sampling theorem for bandpass spectra, the largest integer not exceeding f_{max}/W with bandwidth W =100 Hz is m = 1. Thus, the minimum sampling rate is:

$$f_s = \frac{2f_{\max}}{m} = \frac{2 \cdot 125Hz}{1} = 250Hz \tag{3.29}$$

The minimum sampling rate of our chirp signal is actually the Nyquist frequency. For the simulations, a sampling rate of 512 Hz is chosen. Figure 3.11 depicts graphically the signal spectra for the sampled chirp signals.

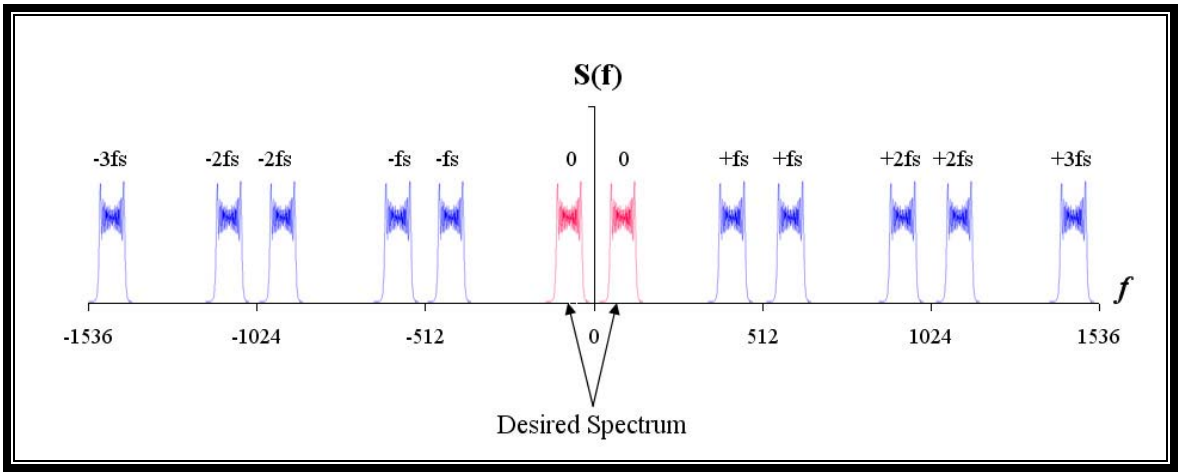

Figure 3.11 – Spectrum of sampled chirp signal

4. SIMULATIONS RESULTS

In this chapter, the simulation models and results are presented. The chirp modulation signals are simulated over four different underwater channel models. Each channel is discussed in detail in what follows. We first discuss the simulation in general and then we proceed to present the simulation model and results of CSK with additive white Gaussian noise (AWGN), $n_g(t)$, only. The next section expands the first model by introducing two multipath signals to the system to simulate time delay (or ISI) and Doppler spread. These multipath signals include delay in time, τ, shift in phase, φ, and shift in frequency, v. For simplicity, these parameters – τ, φ, v – are constant throughout our simulations.

After that, the author expands the model by introducing the Rayleigh amplitude fading, $A_r(t)$. All simulations and results for the third simulation model are discussed in this section. The fourth and last simulation model includes AWGN, Rayleigh amplitude fading, and multipath. The last section of this chapter compares the performance of all our simulations and issues in simulations.

A general, parameterized model of the presented CSK system in four different channel models has been implemented using Matlab-Simulink 5 (Release 13). All blocks are obtained from the Simulink library.

4.1 SYSTEM MODEL IN SIMULINK

All four systems in this thesis utilize the same transmitter and receiver model, with different channel models. In this section, the transmitter and receiver models are briefly explained.

4.1.1 Transmitter

The transmitter block contains the *random integer generator block*, and *the chirp signal generator block* (see Figure 4.1). The random integer generator block generates uniformly distributed random integers of 1 and 0 with a period of $T = 1$. The chirp signal generator block generates the linear-up-chirp signal and the linear-down-chirp signal. The switch determines the corresponding chirp signal for every bit integer number produced by the random integer generator block. The 1's correspond to the up-chirp and the 0's correspond to the down-chirp.

The parameters of chirp signals used in the simulations are:

Sampling rate, T_s: 1/512 samples per T

Minimum frequency, f_{min}: 25 Hz

Maximum frequency, f_{max}: 125 Hz

Slope/chirp rate, μ: 100 Hz/T

The up- and down-chirp signals then:

$$s_u(t) = \cos\left(50\pi t + 100\pi t^2\right) \tag{4.1a}$$

$$s_d(t) = \cos\left(250\pi t - 100\pi t^2\right) \tag{4.1b}$$

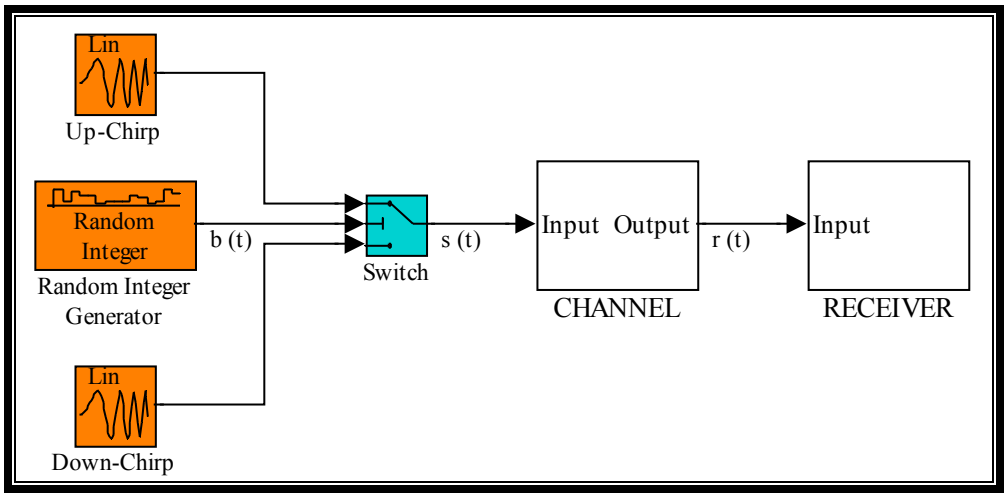

Figure 4.1 – Block diagram of the CSK transmitter (colors)

4.1.2 Receiver

At the receiver (see Figure 4.2), the received signal, *r(t)*, is multiplied by an up chirp; this operation is performed by the *chirp-up* and *product blocks*. The resulting signal is then integrated at the *integrate-and-dump block*, essentially performing a simple, first order low pass filter. This block integrates the input signal in discrete time and resets to zero every period *T*. The *sample-and-hold block* acquires *y(t)* whenever it receives a trigger from the clock and holds the value for a whole period. Here, the *clock* is set to the end of each period. Because the output of the sample-and-hold block has to wait for a whole period, the predicted data, $\hat{b}(t)$, is delayed by one period, *T*. Figure 4.2 illustrates the entire receiver structure.

Figure 4.3 shows an example of the integrated signal, *y(t),* for every corresponding source data *b(t)* over five signaling intervals. Figure 4.4 shows the results of the sample and hold operations. The line in yellow is the integrated signal. The line in pink is the sampled and held signal. All values equal or greater than ¼ are decoded to be $\hat{b}(t) = 1$, and all values less than ¼ are decoded to be $\hat{b}(t) = 0$.

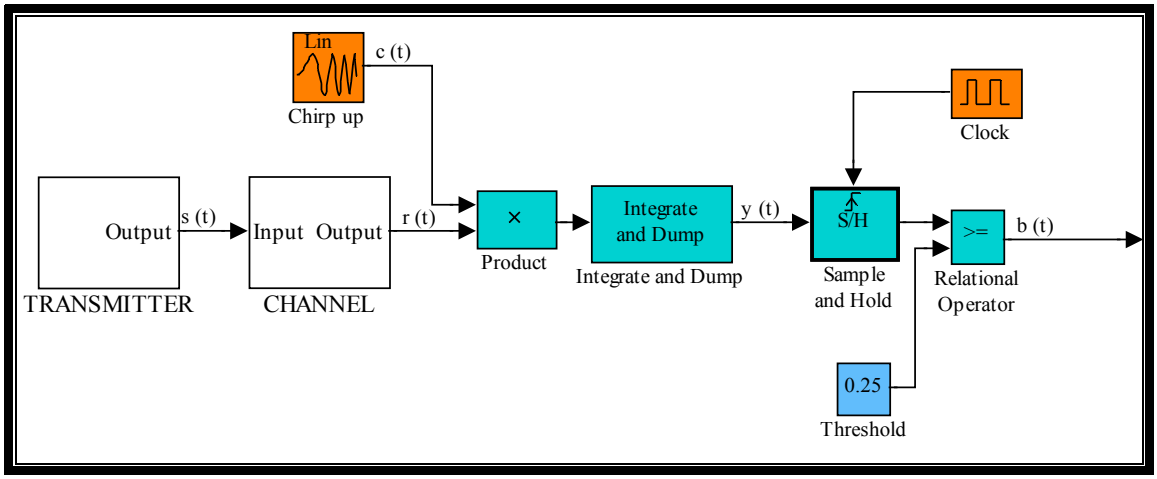

Figure 4.2 – Block diagram of the CSK receiver (colors)

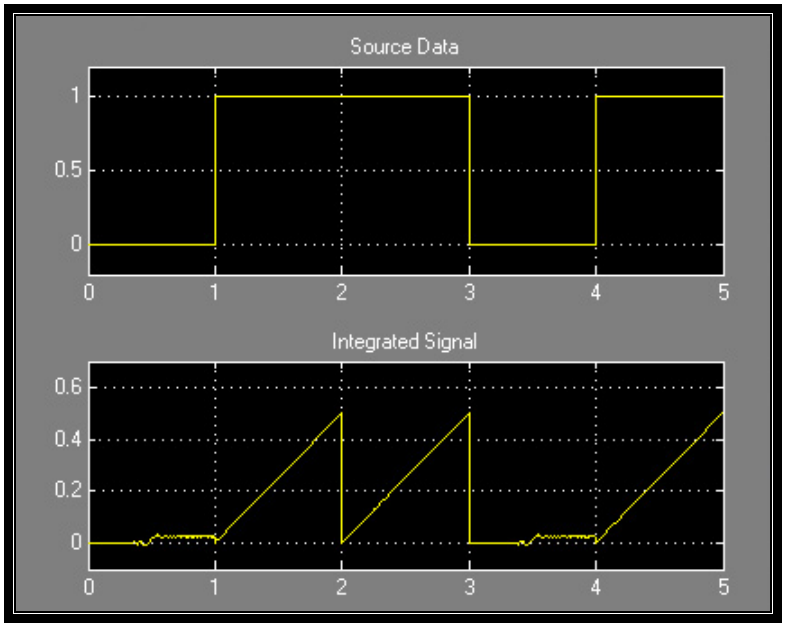

Figure 4.3 – Transmitted (top) and integrated received signal (bottom)

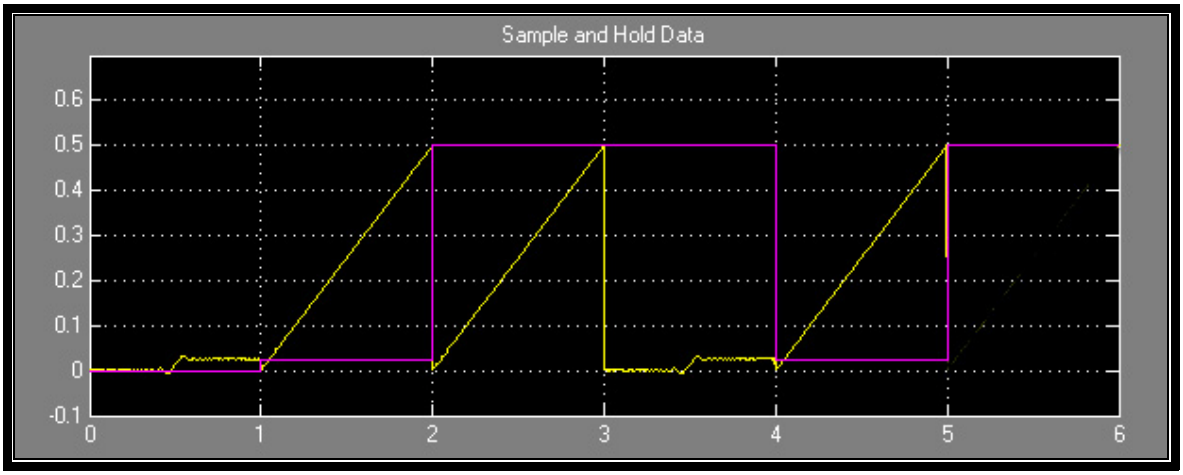

Figure 4.4 – Sample and hold data (pink) and integrated data (yellow)

The simulated BER curves were obtained by computing the probability of error after at least 10 bits errors, for each SNR values selected:

$$P_b(e) = \frac{Errors}{total\ symbols\ transmit} \tag{4.2}$$

The computing time to simulate each BER point ranged from several minutes up to several days, depending on the SNR value, defined in Eq. (2.17) and (2.24), and the computer's speed and memory capacity.

4.2 MODEL 1: SIMULATIONS WITH ADDITIVE WHITE GAUSSIAN NOISE (AWGN)

The first channel is modeled by Additive White Gaussian Noise (AWGN). The received signal can be written as follows:

$$r(t) = s(t) + n_g(t) \tag{4.3}$$

Again, $n_g(t)$ is the Gaussian noise with the PDF in Eq. (2.14). Replacing $s(t)$ with Eq. (3.14a,b), Eq. (4.3) becomes:

$$r(t) = \cos\left(2\pi ft \pm \pi\mu t^2\right) + n_g(t) \tag{4.4}$$

where the positive slope corresponds to a transmitted 1 and the negative slope to a 0.

We define the SNR as in Eq (2.17) with E_s as the energy of s_u or s_d of approximately 0.5.

Figure 4.5 shows the complete diagram of the system with the A*dditive White Gaussian Noise channel* block included (block in blue); and Figure 4.6 shows the bit error rate versus the signal to noise ratio graph of the CSK in the AWGN channel. The

graph shows an outstanding performance. The system is able to achieve a BER of $1x10^{-3}$ with an SNR of 13 dB. The simulation values of Figure 4.6 are listed in Appendix 7.3.

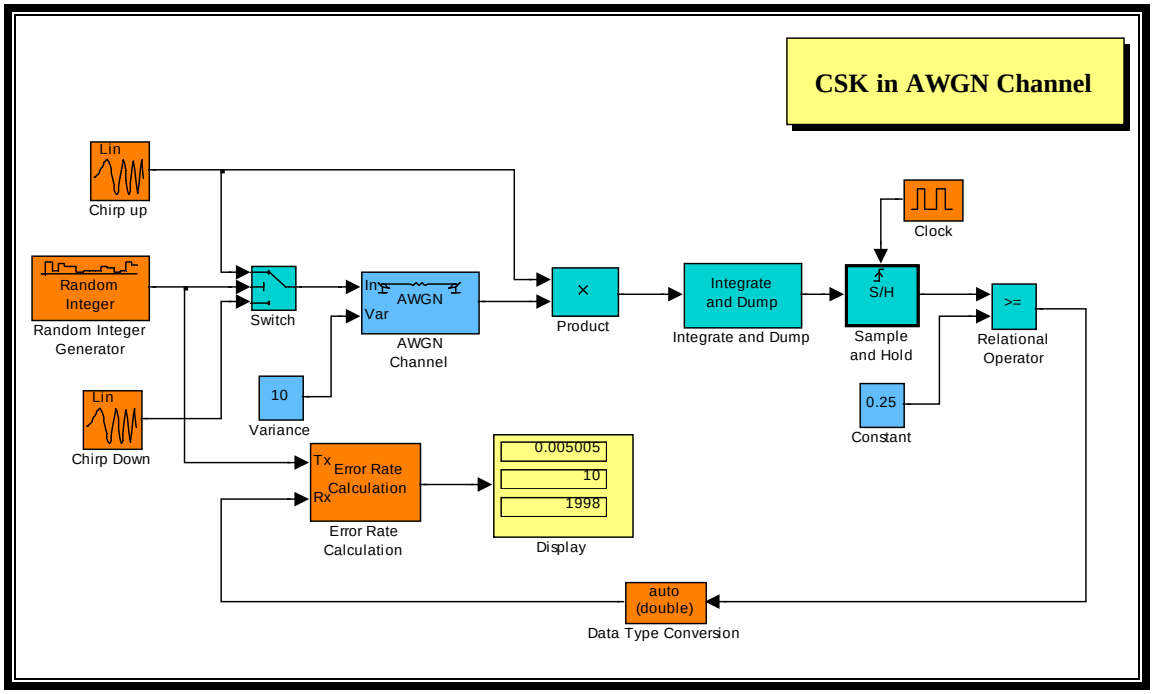

Figure 4.5 – CSK in AWGN Channel

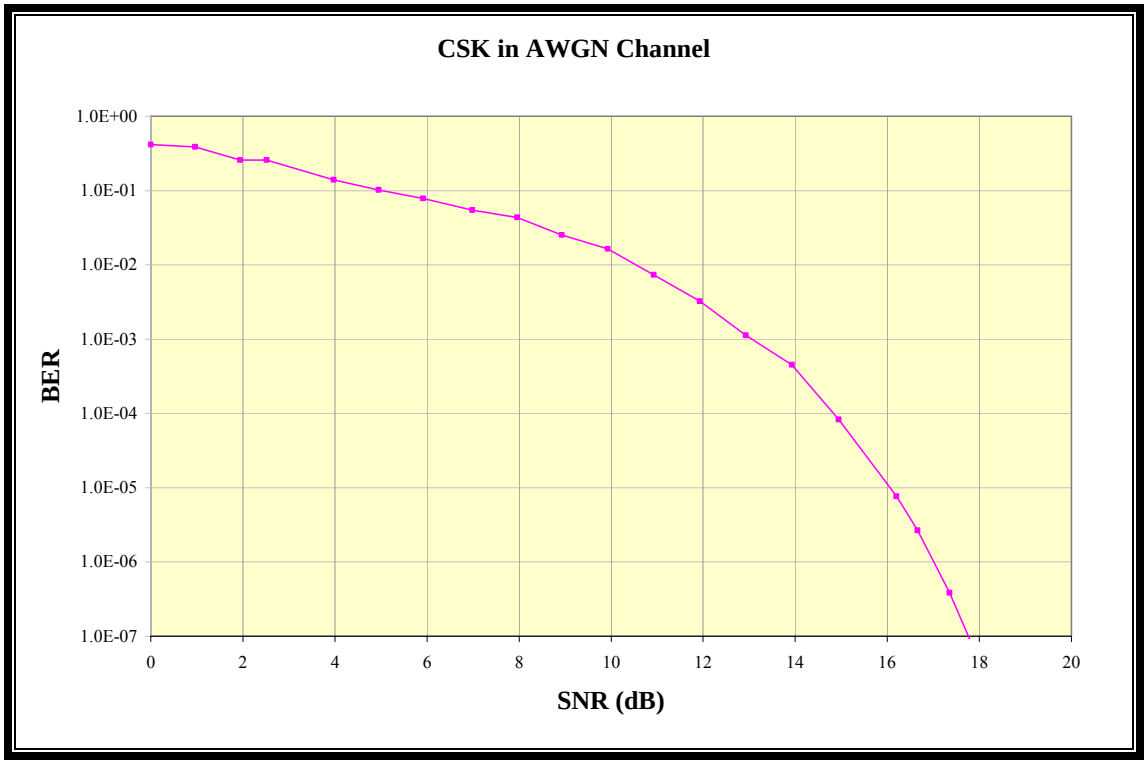

Figure 4.6 – BER of CSK in AWGN Channel

4.3 MODEL 2: SIMULATIONS WITH ADDITIVE WHITE GAUSSIAN NOISE AND MULTIPATH

The second channel is affected by Additive White Gaussian Noise (AWGN) and also ISI of two delayed signals. The interfering signals are shifted both in time and frequency (Doppler) and contain a shift in phase, resulting in a received signal spread in time and frequency:

$$r(t) = r_0(t) + r_1(t + \tau_1, \varphi_1, f + \nu_1) + r_2(t + \tau_2, \varphi_2, f + \nu_2) \tag{4.5}$$

$$r_0(t) = \cos(2\pi ft \pm \pi\mu t^2) + n_g(t) \tag{4.6}$$

$$r_1(t) = \alpha_1 \cos(2\pi(f + \upsilon_1)(t + \tau_1) \pm \pi\mu(t + \tau_1)^2 + \varphi_1) \tag{4.7}$$

$$r_2(t) = \alpha_2 \cos(2\pi(f + \upsilon_2)(t + \tau_2) \pm \pi\mu(t + \tau_2)^2 + \varphi_2) \tag{4.8}$$

where τ is the time shift, φ is the phase shift, υ is the frequency shift, α is the amplitude scale, and $n_g(t)$ is the Gaussian noise. The parameters of the two delayed signals used in our simulations are:

1. Delayed Signal 1:
   - Time shift, τ_1: 1024 samples (2 T)
   - Phase shift, φ_1: 30 degrees
   - Frequency shift, υ_1: 20 Hz
   - Gain, α_1: -3 dB
2. Delayed Signal 2:
   - Time shift, τ_2: 4000 samples (7.8 T)
   - Phase shift, φ_2: 20 degrees
   - Frequency shift, υ_2: 50 Hz
   - Gain, α_2: -6 dB

These shift values are chosen somewhat arbitrarily.

We define the SNR as in Eq (2.17) with E_s as the energy of s_u or s_d of approximately 0.5.

Figure 4.7 shows the complete diagram of the system with the *additive white Gaussian noise channel* block with delayed interference from multipath. Figure 4.8 depicts details of the *multipath* block, clearly showing the addition of two delayed, amplitude scaled, phase and frequency shifted signals to the direct path signal.

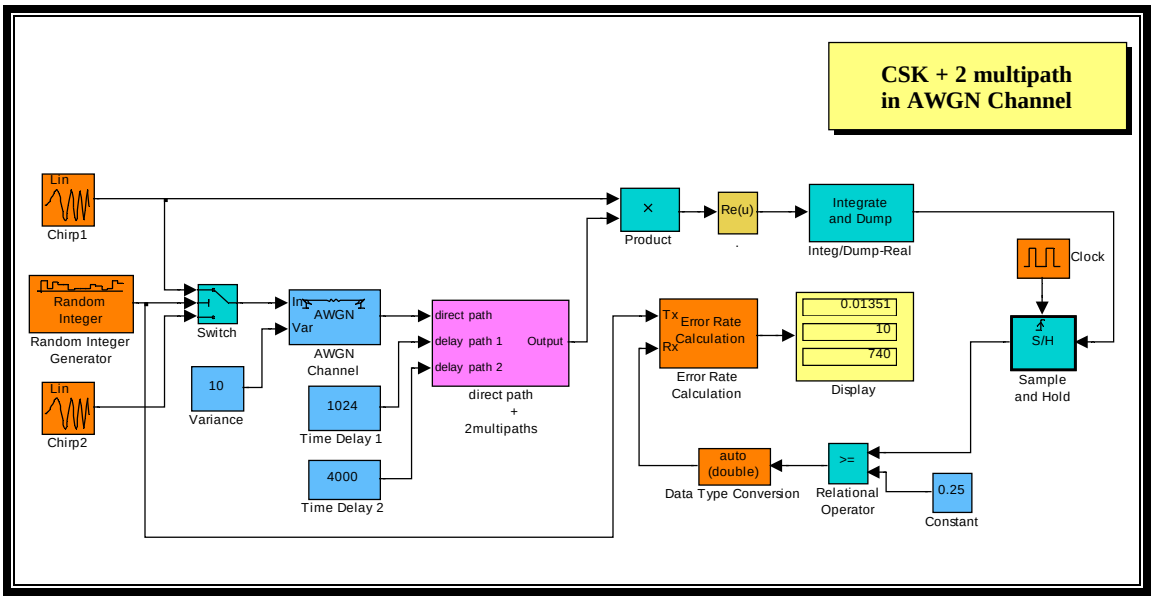

Figure 4.7 – CSK in AWGN Channel with multipath

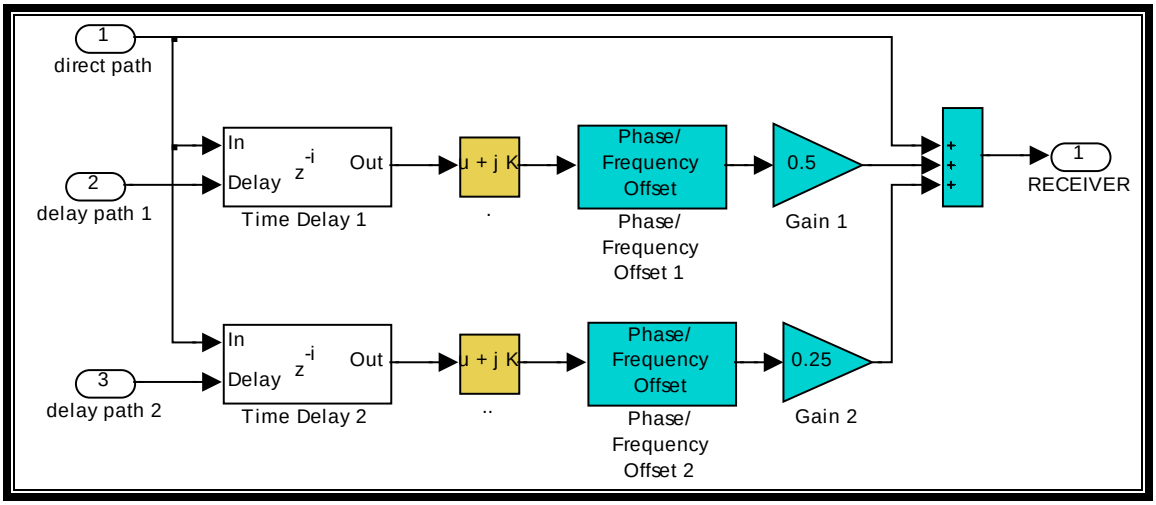

Figure 4.8 – Direct path and multipath

Figure 4.9 shows the bit error rate versus the signal to noise ratio graph of the CSK in the AWGN channel. The graph shows an excellent performance. The system is able to achieve a BER of $1x10^{-3}$ with an SNR of 15 dB, a 2 dB degradation from the first model without multipath. The simulation point values of Figure 4.9 are listed in Appendix 7.3.

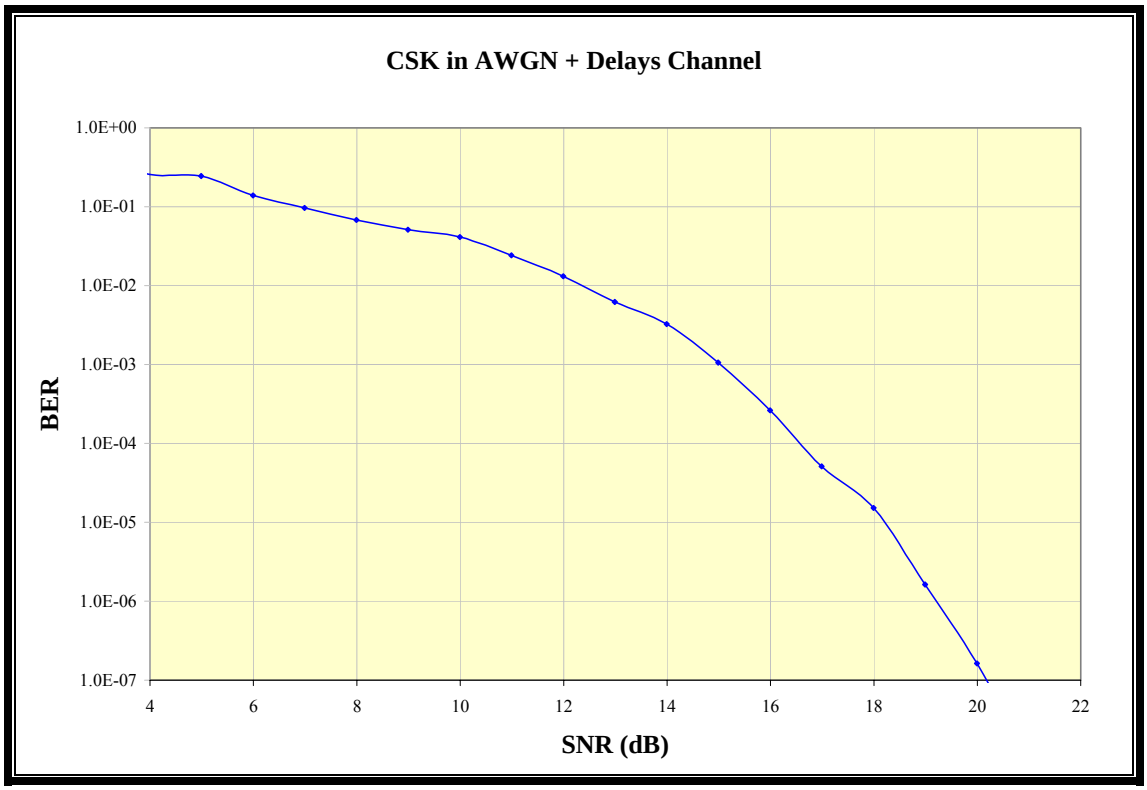

Figure 4.9 – BER of CSK in AWGN and multipath

4.4 MODEL 3: SIMULATIONS WITH ADDITIVE WHITE GAUSSIAN NOISE AND RAYLEIGH AMPLITUDE FADING

The third channel is modeled by the Additive White Gaussian Noise (AWGN) and the Rayleigh amplitude fading:

$$r(t) = A_r(t)\left[s(t) + n_g(t)\right] \tag{4.9}$$

$$r(t) = A_r(t)\left[\cos(2\pi ft \pm \pi\mu t) + n_g(t)\right] \tag{4.10}$$

where again $n_g(t)$ is the Gaussian noise and $A_r(t)$ represents the Rayleigh fading with the PDF given in Eq. (2.18).

Figure 4.10 shows the complete diagram of the system with the *Additive White Gaussian Noise channel* block and the *Rayleigh fading distribution generator block* included. Figure 4.11 shows the bit error rate versus the signal to noise ratio graph of the CSK in the AWGN channel with Rayleigh fading, for two different values of the fading parameter, σ. The graph also shows that CSK achieves excellent performance. With $\sigma = 1$ (red line) for the Rayleigh parameter, the system is able to achieve a BER of $1x10^{-3}$ with an SNR of 15 dB. Also seen in Figure 4.11 is that for SNR smaller than about 11 dB, the Rayleigh parameter values does not influence average BER, while for smaller SNR the BER is increased as much as two orders of magnitude. The simulation results of Figure 4.11 are tabulated in Appendix 7.3.

The SNR is defined as in Eq (2.24) with E_s as the energy of s_u or s_d and a_r as the energy of Rayleigh fading of approximately -3 dB for $\sigma = 1$, and about -8 dB for $\sigma = 0.5$.

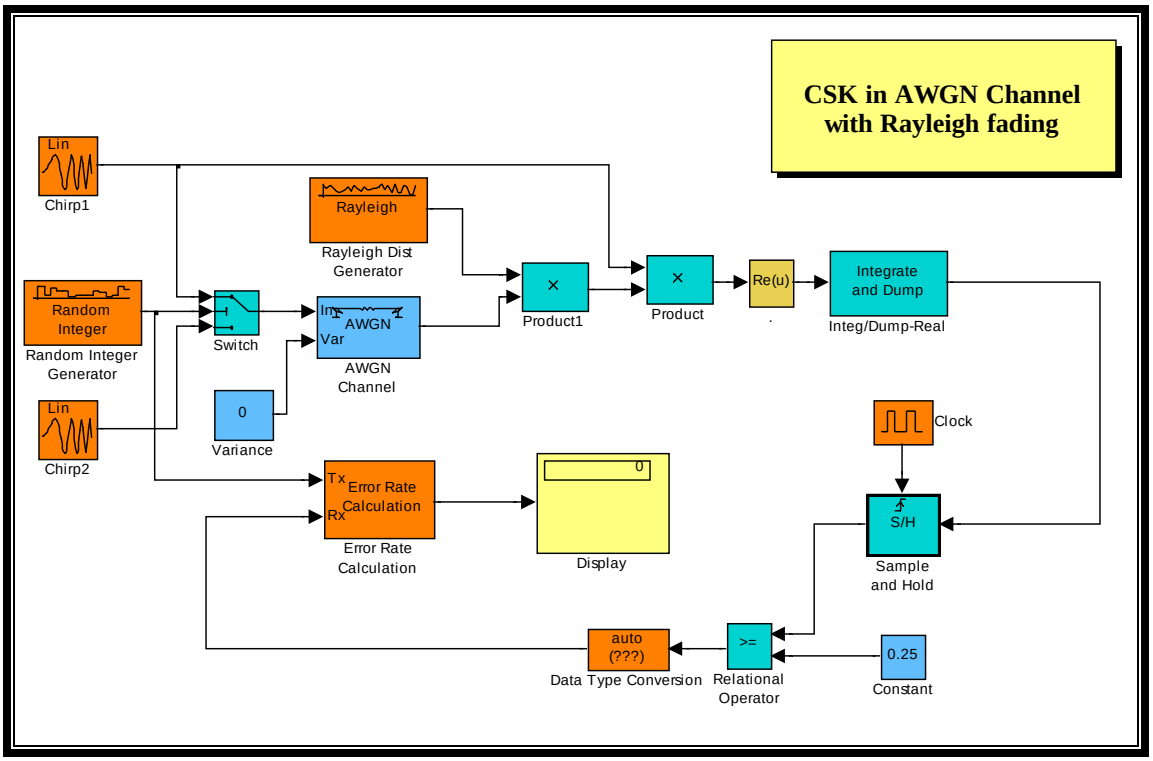

Figure 4.10 – CSK in AWGN Channel with Rayleigh fading

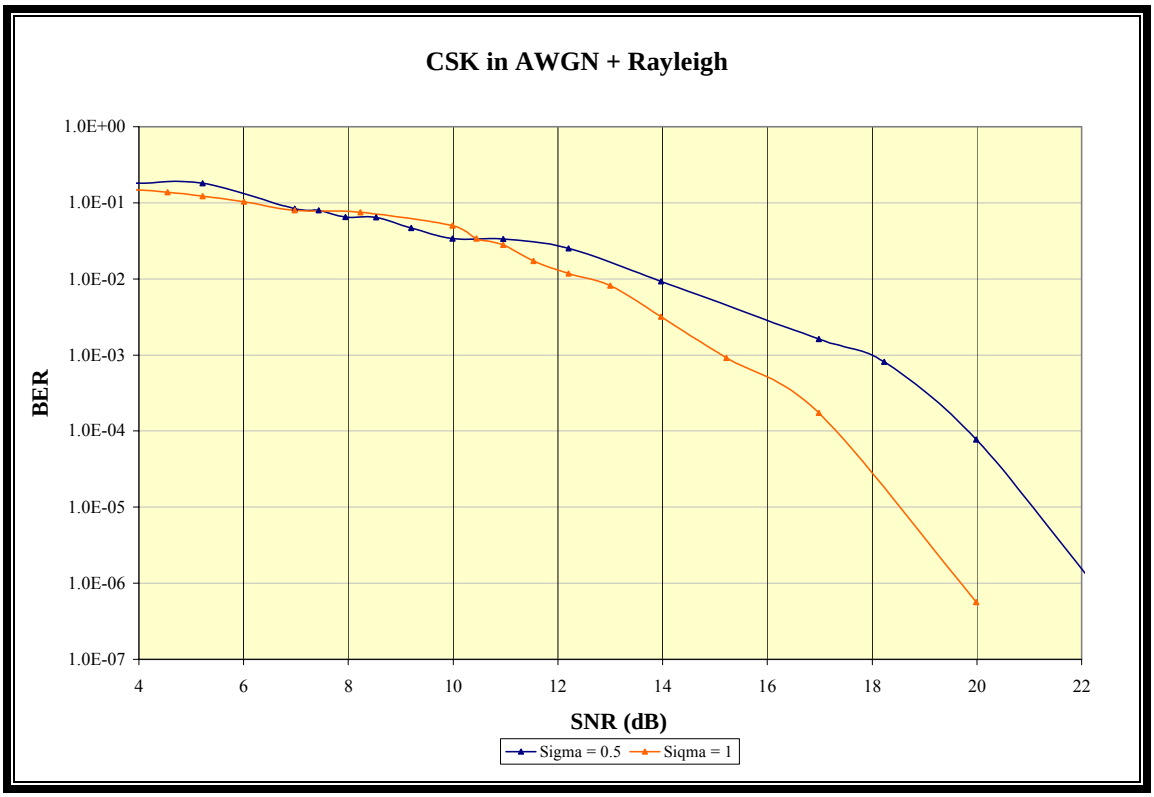

Figure 4.11 – BER of CSK in AWGN channel with Rayleigh fading

4.5 MODEL 4: SIMULATIONS WITH ADDITIVE WHITE GAUSSIAN NOISE, RAYLEIGH FADING, AND MULTIPATH

The fourth, most complex, and probably most realistic channel model includes additive white Gaussian noise (AWGN), Rayleigh fading, and also multipath (two delayed signals added to the direct path).

$$r(t) = A_r(t)\left[r_0(t) + r_1(t+\tau_1, \varphi_1, f+\nu_1) + r_2(t+\tau_2, \varphi_2, f+\nu_2) + n_g(t)\right] \tag{4.11}$$

where τ is the time shift, φ is the phase shift, and υ is the frequency shift. The signals r_0, r_1, and r_2, were defined in Eq. (4.6), (4.7), and (4.8). This model uses the same delayed signals that were described in Section 4.3. For convenience, the parameters of those two delayed signals are listed below again.

1. Delayed Signal 1: Time shift, τ_1: 1024 samples (2 T)
   Phase shift, φ_1: 30 degree
   Frequency shift, υ_1: 20 Hz
   Gain, α_1: -3 dB
2. Delayed Signal 2: Time shift, τ_2: 4000 samples (7.8 T)
   Phase shift, φ_2: 20 degree
   Frequency shift, υ_2: 50 Hz
   Gain, α_2: -6 dB

Figure 4.12 shows the complete diagram of the system with the *Additive White Gaussian Noise channel* block, the *Rayleigh fading distribution generator* block and the multipath included. Figure 4.13 illustrates the bit error rate of CSK versus the signal to noise ratio. Again, the graph shows excellent performance, even in this deleterious channel. The system is able to achieve a BER of $1x10^{-3}$ with an SNR of 16.5 dB with

σ = 1 (green line) for the Rayleigh parameter. Once again, we see that the Rayleigh parameters σ influences the performance only to SNR above 14 dB only. The simulated values of Figure 4.13 are listed in Appendix 7.3.

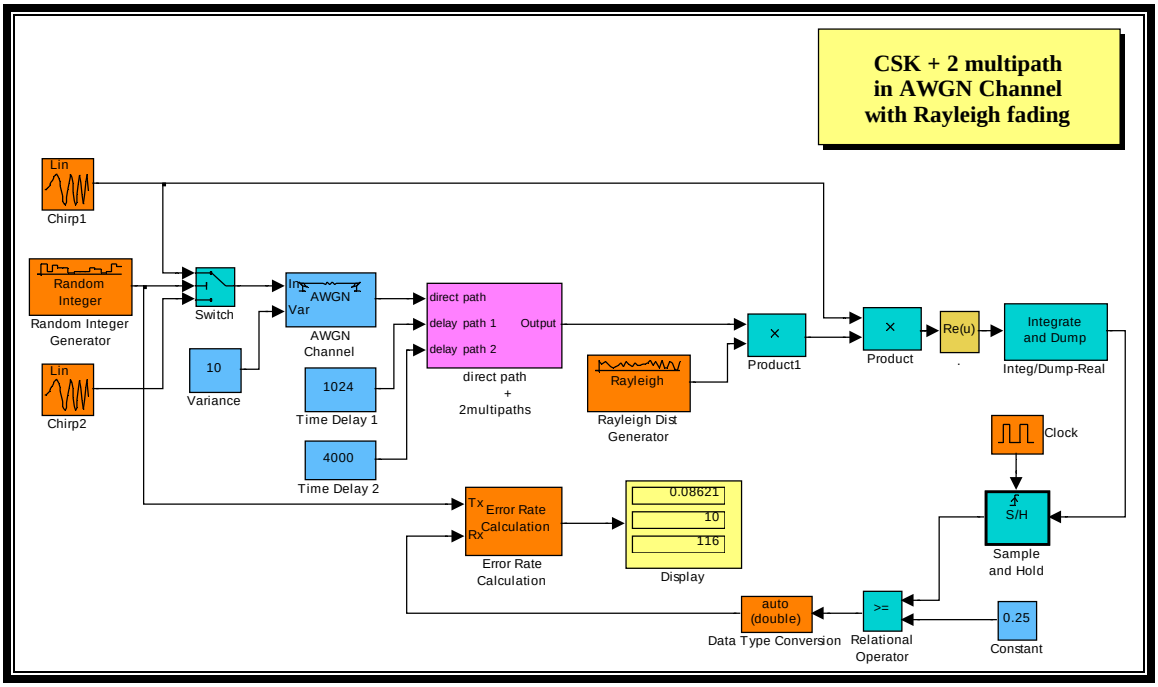

Figure 4.12 – CSK in AWGN Channel with Rayleigh fading and multipath

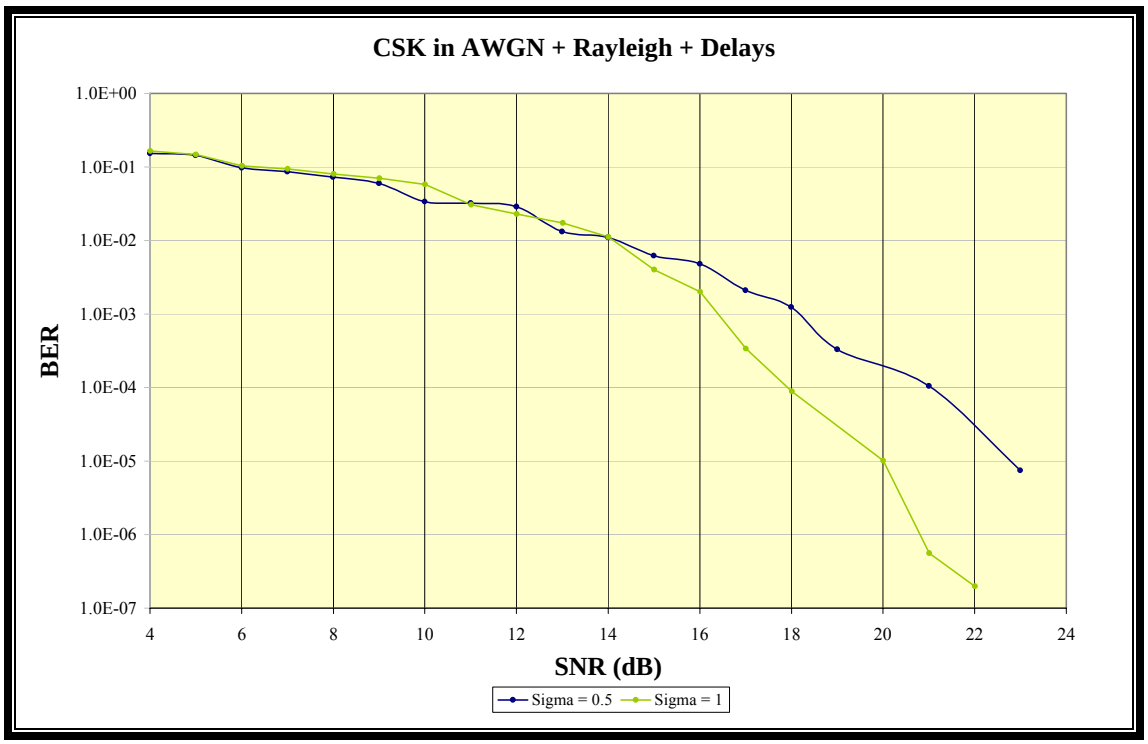

Figure 4.13 – BER of CSK in AWGN Channel with Rayleigh fading and multipath

4.6 COMPARISON OF RESULTS FOR ALL SIMULATIONS

To complete this chapter, we compare and discuss all results. The BER curves for all channel models are shown in Figure 4.14. The pink line curve is for the channel with AWGN only, the most benign channel. The blue line curve is for the channel with the Gaussian noise and multipath signals. The curve in red is for the channel with the Gaussian noise and the Rayleigh fading with Rayleigh parameter of $\sigma = 1$. The last curve in green is the channel with Gaussian noise, Rayleigh fading ($\sigma = 1$), and multipath signals. The BER and SNR values of these four channel models are listed in Table 4.1, for 2 significant values of BER.

Table 4.1 – Significant BER vs. SNR points for all models

Channel	BER	SNR (dB)	BER	SNR (dB)
CSK in AWGN	$1x10^{-3}$	13	$1x10^{-6}$	17
CSK in AWGN + Multipath	$1x10^{-3}$	15	$1x10^{-6}$	19.2
CSK in AWGN + Rayleigh	$1x10^{-3}$	15	$1x10^{-6}$	19.7
CSK in AWGN + Rayleigh + Multipath	$1x10^{-3}$	16.5	$1x10^{-6}$	20.7

Overall, the performance degrades by about 2 dB when delays are included to represent multipath for BER of $1x10^{-3}$ and smaller, from the AWGN. We can see that at BER of $1x10^{-3}$, the SNR of AWGN with multipath is smaller by approximately 2 dB from AWGN alone, and the SNR of the AWGN and Rayleigh fading with multipath is also smaller approximately by 1.5 dB from the AWGN and Rayleigh fading. By introducing Rayleigh fading to the AWGN channel, the BER performance degrades by

approximately 2 dB. Here we can make an assumption that the effect of the Doppler and the Rayleigh fading contribute the same degradation to the AWGN channel.

Figure 4.15 shows the BER performance of CSK and BPSK in two different channels. The first channel is the AWGN channel and the second one is the AWGN and Rayleigh amplitude fading. Both signals utilize the same demodulation method. The solid lines are results for CSK and the dashed lines are for BPSK.

In AWGN channel, the graph shows the performance of CSK is worse from BPSK by approximately 6 dB for BER of $1x10^{-3}$ as expected. The output of the integrate-and-hold for BPSK is either + ½ or - ½ for data of 1 or 0 respectively, whereas the output for CSK is either + ½ or 0 for data 1 or 0, respectively. There is ½ difference in magnitude, or 6 dB difference in power. However, CSK is more desirable because by adding Rayleigh amplitude fading to the channel, the BPSK performance degrades tremendously compared to CSK. With the fact that the channel with Rayleigh amplitude fading is more realistic, the CSK excels over BPSK even with the sub-optimal integrate-and-dump receiver. This improvement is expected to be more drastic when better receivers are used.

4.7 SAMPLING RATE AND LOWPASS FILTER

Choosing the optimal sampling rate proved to be a difficult task. According to the sampling theory described in Section 3.3.3, as long the sampling rate is greater than the Nyquist rate, the continuous signal should be recovered exactly from the sampled version. However, as we can see from Figure 4.16, the BER obtained in our simulations depends on the sampling rate. As we increased the sampling rate, the BER converges to an "optimal" value. By increasing the sampling rate from the Nyquist rate to 512

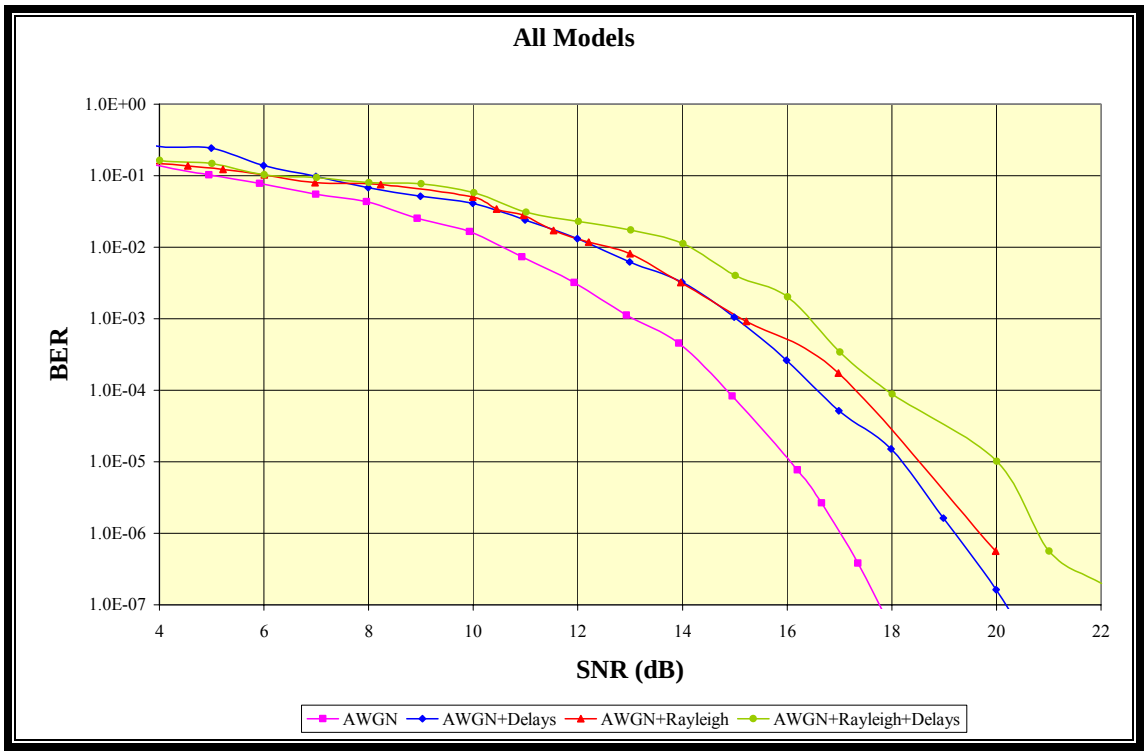

Figure 4.14 – BER of CSK in various channels

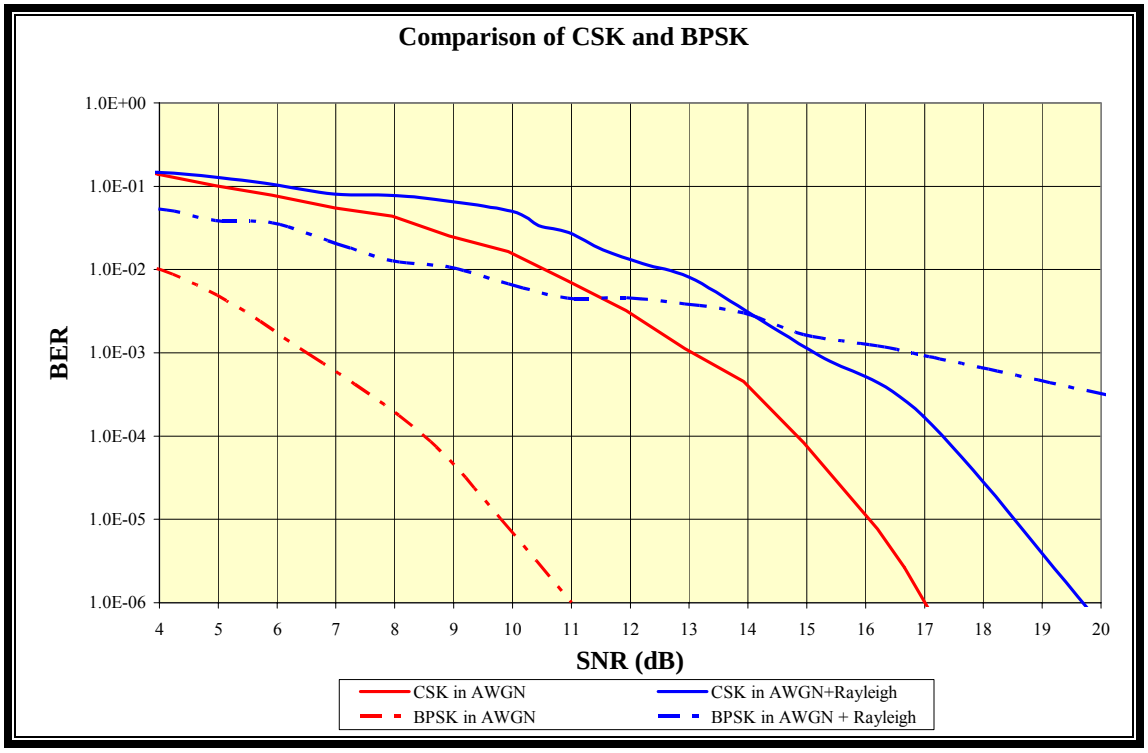

Figure 4.15 – BER of CSK and BPSK

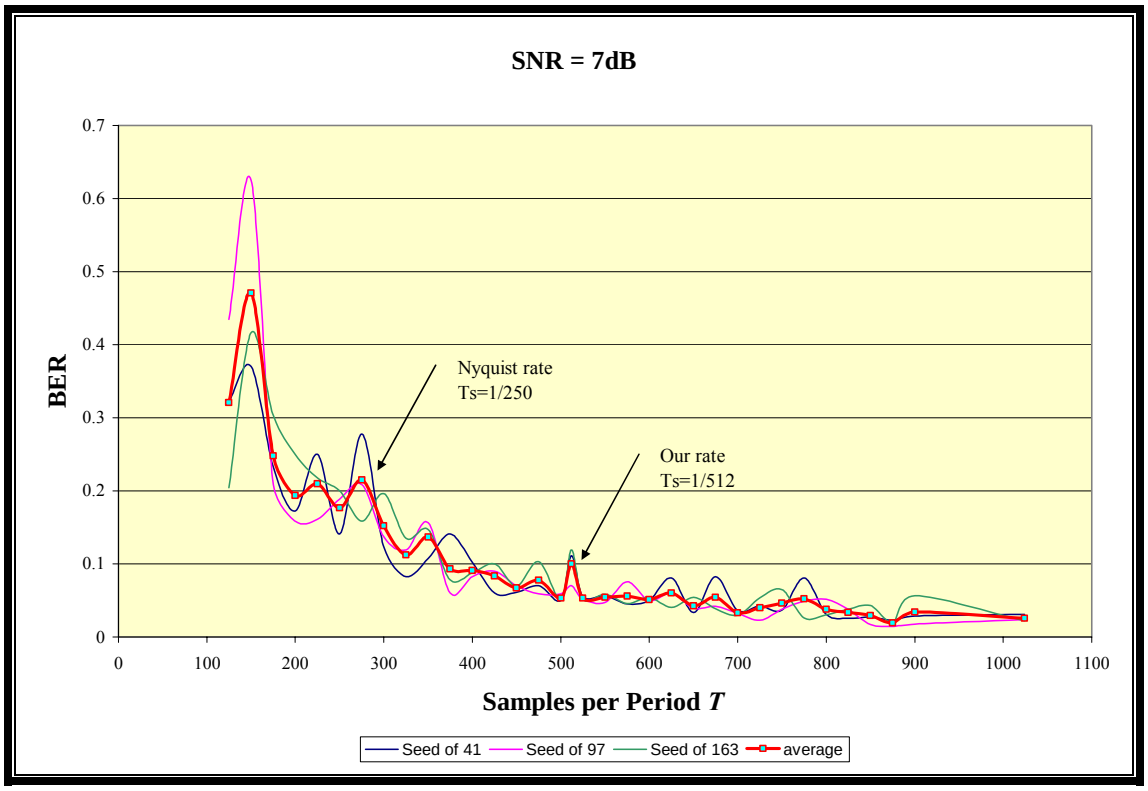

Figure 4.16 – Sampling rate analysis in AWGN channel

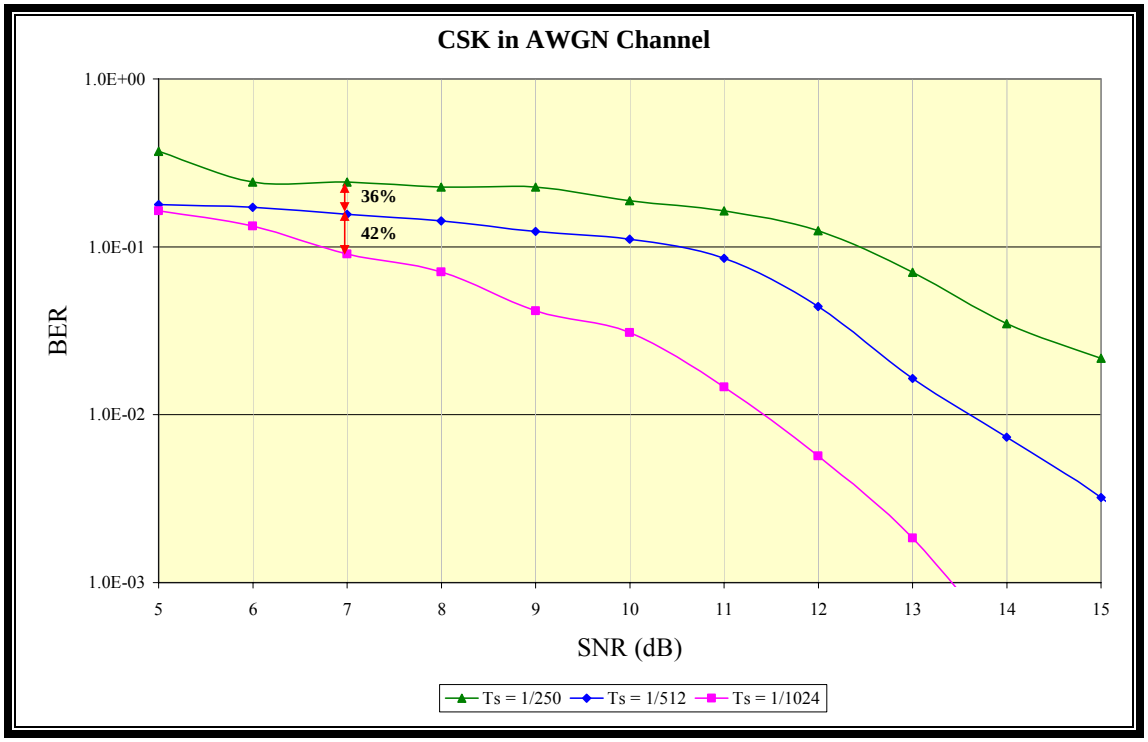

Figure 4.17 – BER curves with different sampling rate in AWGN channel

samples per period, on average, the BER improves approximately by 36%; and from 512 samples per period to 1024 samples per period, the BER improves approximately by 42% (see Figure 4.17).

The BER values depicted in Figure 4.16 are obtained from the AWGN channel with SNR of 7 dB. The seed numbers in the graph refer to the pseudorandom number generator in the AWGN block. The line in bold red is the average of error rate over three samples. Each point was computed by counting 10 errors.

It turns out that the degradation of the BER performance is not due to the lower sampling rate, but due to the filter used. An integrator is the simplest pass filter mathematically. The transfer function of an integrator is:

$$H(s) = \frac{1}{s} \tag{4.10}$$

It has a single pole at zero on the jω and therefore filter's transient response is long. The integrator's gain diminishes with increasing frequency. The gain is inversely proportional to frequency; it has a slope of -1 or -20 dB/decade on a Bode plot as shown in Figure 4.18. By setting the cutoff frequency of the filter to $f_c << 2\pi B$, the magnitude of chirp is greatly diminished; and this is what is affecting the BER performance.

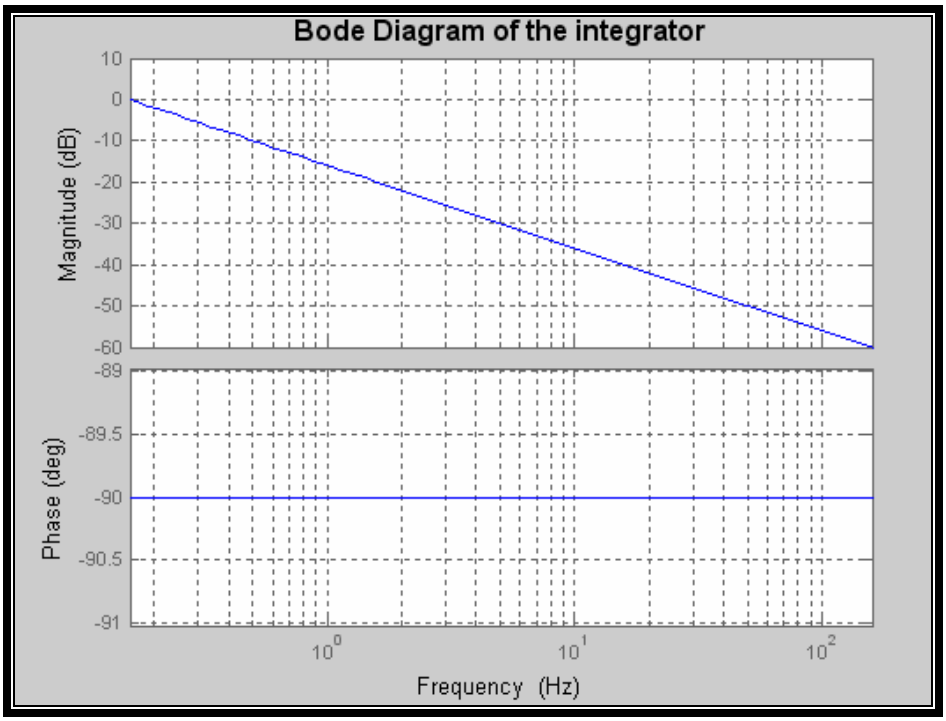

Figure 4.18 – Bode plot of an integrator

5. CONCLUSIONS AND SUGGESTION FOR FURTHER WORK

This thesis proposed a digital modulation method using Chirp Slope Keying (CSK) for coherent underwater acoustic communications. To understand the importance of a reliable detection system underwater, we reviewed in detail the underwater channel conditions. We then presented a general model of chirp signaling and linked this to the proposed CSK transmission system. The mathematical model of the system was presented. By implementing a first order filter with an integrate-and-dump at the receiver, we showed good quality of detection of the transmitted binary signal. The system was simulated in four different statistical underwater channel models. These channel models consisted of the additive white Gaussian noise, the Rayleigh fading, and multipath signals with shifts in time, phase, and frequency. The BER curves versus SNR were presented and clearly demonstrate the feasibility of CSK for digital transmission underwater.

More improvement of Binary CSK over other standard digital modulation schemes is expected as channel conditions deteriorate. PSK is very sensitive to phase shift and Rayleigh amplitude. FSK is extremely sensitive to frequency shift and frequency selective fading. ASK cannot handle amplitude fading. Even though CSK is about 6 dB worse in the most benign AWGN channel, this deficit decreases as channel conditions worsen. CSK over performs others in these very deleterious channels.

CSK is a promising modulation method for the underwater communication channel. However, more research is needed, especially in the areas of underwater acoustic channel modeling and receiver structures for CSK.

In this thesis, a very simple integrator is used to demodulate the distorted received signals. Implementing different receiver configuration can easily improve the performance of CSK systems. These receiver configurations may include matching filtering receiver or frequency slope detection receiver using, for example, the Hough Transform.

Expanding Binary CSK to Quadrature CSK (QCSK) for transmission at 2 bits/sec/Hz can easily be done by allowing doubling the number of available slopes in the chirps; this doubles the number of bits transmitted per signaling interval. CSK can also be extended to M-ary CSK for transmission at $\log_2(M)$ bits/sec/Hz to have a more efficient use of bandwidth.

Future research is open to the improvement in the channel modeling. In this thesis, many of the multipath parameters (the time shift, phase shift, frequency shift, and gain) were chosen somewhat arbitrarily. Randomization of these parameters, using appropriate distributions will create a more realistic channel model and more accurate average performance characterization. Experimental data needs to be collected to validate the channel models. Including Doppler spread to the system is a promising research area that must be investigated further to prove that CSK is virtually insensitive to Doppler.

The performance of any communication system is heavily dependent on the internal and external synchronizations. Throughout this thesis we assumed that both synchronizations are achieved without error. However, this assumption is unrealistic. So

another possible future research area would concentrate on determining the degradation of the system performance due to synchronization errors.

6. REFERENCES

[1] M. Stojanovic, "Underwater acoustic communications," *IEEE Electro International,* pp. 435-440, June 1995.

[2] W. S. Burdic, "Underwater acoustic system analysis," Prentice Hall, 1991.

[3] A. B. Baggeroer, "Acoustic telemetry – An overview," *IEEE Journal of Oceanic Engieering,* Vol. OE-9, No. 4, pp. 229-235, October 1984.

[4] E. MacCurdy, "The notebooks of Leonardo da Vinci," Garden City Publishing Co., Inc., Chapter X, 1942.

[5] D. B. Kilfoyle, A. B. Baggeroer, "The state of the art in underwater acoustic telemetry," *IEEE Journal of Oceanic Engineering,* Vol. 25, No.1, pp 4-27, January 2000.

[6] A. Essebbar, G. Loubet, F. Vial, "Underwater acoustic channel simulations for communication," *IEEE Oceans 1994,* Vol. 3, pp. III/495-III/500, September 1994.

[7] D. Middleton, "Channel modeling and threshold signal processing in underwater acoustics: An analytical overview," *IEEE Journal of Oceanic Engineering,* Vol. OE-12, No. 1, pp. 4-28, January 1987.

[8] H. V. Poor, "Uncertainty tolerance in underwater acoustic signal processing," *IEEE Journal of Oceanic Engineering,* Vol. OE-12, No.1, pp. 48-65, January 1987.

[9] M. Johnson, J. Preisig, L. Freitag, M. Stojanovic, "FSK and PSK performance of the utility acoustic modem," *Oceans 1999MTS/IEEE Proceedings,* Vol. 3, pp 1512-1515, September 1999.

[10] T. Eggen, A. Baggeroer, J. Preisig, "Communication over Doppler spread channels – Part I: Channel and receiver presentation," *IEEE Journal of Oceanic Engineering,* Vol. 25, No.1, pp. 62-71, January 2000.

[11] T. Eggen, A. Baggeroer, J. Preisig, "Communication over Doppler spread channels – Part II: Receiver characterization and practical results," *IEEE Journal of Oceanic Engineering,* Vol. 26, No.4, pp. 612-621, October 2001.

[12] R. C. Dixon, "Spread spectrum systems," Wiley-Interscience, 1976.

[13] S. Hengstler, *A Novel Chirp Modulation Spread Spectrum Technique For Multiple Access,* M.S. Thesis, University of Massachusetts Dartmouth, January 2001.

[14] J. Holmes, "Spread Spectrum Communication," *Chapter in McGraw-Hill Encyclopedia of Science and Technology,* Ed. 8, Vol.17, pp.271-273, 1997.

[15] J. R. Klauder, A. C. Price, S. Darlington, W. J. Albersheim, "The theory and design of chirp radars," *Journal of Bell Syst. Tech.,* Vol. 39, pp. 745-808, 1960.

[16] M. R. Winkler, "Chirp signals for communications," *WESCON Convention Record,* Paper 14.2, 1962.

[17] A. J. Berni, W. D. Greeg, "On the utility of chirp modulation for digital signaling," *IEEE Transactions on Communications,* Vol.21, No.6, pp.748-751, June 1973.

[18] C. E. Cook. "Linear FM signal formats for beacon and communication systems," *IEEE Transactions on Aerospace and Electronic Systems,* Vol. AES-10, No. 4, pp. 471-478, July 1974.

[19] S. E. El-Khamy, S. E. Shaaban, E. A. Thabet, "Partially coherent detection of continuous phase chirp (CPCM) signals," *Thirteenth National Radio Science Conference,* pp. 485-495, March 1996.

[20] S. E. El-Khamy, S. E. Shaaban, E. A. Thabet, "Multi-user chirp modulations signals (M-CM) for efficient multiple-access communication systems," *Thirteenth National Radio Science Conference,* pp. 289-297, March 1996.

[21] S. E. El-Khamy, S. E. Shaaban, E. A. Thabet, "Frequency-hopped multi-user chirp modulation (FH/M-CM) for multiple fading channels," *Sixteenth National Radio Science Conference,* pp. C6/1-C6/8, February 1999.

[22] S. E. El-Khamy, S. E. Shaaban, "Efficient multiple access communications using multi user chirp modulation signals," *IEEE 4th International Symposium on Spread Spectrum Techniques and Applications,* Vol. 3, pp.1209-1213, September 1996.

[23] L. R. Leblanc, P. Beaujean, M. Singer, C. Boubli, G. T. Strutt, "Chirp FSK modem for high reliability communication in shallow water," *Oceans 1999 MTS/IEEE Proceedings,* Vol. 1, pp. 222-227, September 1999.

[24] L. R. Leblanc, M. Singer, P. Beaujean, C. Boubli, J. R. Alleyne, "Improved chirp FSK modem for high reliability communications in shallow water," *Oceans 2000 MTS/IEEE Proceedings,* Vol. 1, pp. 601-603, September 2000.

[25] R. J. Urick, "Sound propagation in the sea," Peninsula Publishing, 1982.

[26] C. S. Clay, "Acoustical oceanography: principles and applications," John Wiley & Sons, Inc. 1977.

[27] Maxim, "An introduction to direct-sequence spread-spectrum communications," Maxim Dallas Semiconductor [online] February 20003, http://www.maxim-ic.com/appnotes.cfm/appnote_number/1890 (Accessed: September 2004).

[28] S. Hengstler, D. P. Kasilingam, A. H. Costa, "A novel chirp modulation spread spectrum technique for multiple access," *Proceedings of the IEEE International Symposium on Spread Spectrum Techniques and Applications,* Vol. 1, pp. 73-77, September 2002.

[29] H. R. Raemer, "Radar Systems Principles," CRC Press, Inc., 1997.

[30] P. C. Etter, "Underwater Acoustic Modeling and Simulation," Spon Press, 2003.

[31] R. N. McDonough, A. D. Whalen, "Detection of Signals in Noise," Academic Press, 1995.

[32] W. C. Y. Lee, "Estimate of channel capacity in Rayleigh fading environment," *IEEE Transactions on Vehicular Technology,* Vol. 39, No. 3, pp. 187-189. August 1990.

[33] G. Cook, A. Zaknich, "Chirp sounding the shallow water acoustic channel," *Proceedings of the 1998 IEEE International Conference on Acoustics, Speech, and Signal Processing,* Vol.4, pp. 2521-2524, May 1998.

[34] R. E. Ziemer, W. H. Tranter, "Principles of Communications: Systems, Modulation, and Noise," Houghton Mifflin, 1976.

[35] D. Dahlhaus, "Chirp Modulation," *Chapter in Wiley Encyclopedia of Telecommunications,* Vol.1, pp.440-448, 2003.

[36] L. Simanjuntak, "Investigation of Underwater Communications," Paper for Independent Study ENEE 4096 course, 2002

7. APPENDICES

7.1 MATHEMATICAL DERIVATION OF THE ORIGINAL MODEL

Definition:

Up-Chirp: $S_U(t) = \exp\left[j\left(\frac{a}{2} t^2 + bt \right) \right] = \cos\left(\frac{a}{2} t^2 + bt \right) + j \sin\left(\frac{a}{2} t^2 + bt \right)$

Down-Chirp: $S_D(t) = \exp\left[j\left(-\frac{a}{2} t^2 + bt \right) \right] = \cos\left(-\frac{a}{2} t^2 + bt \right) + j \sin\left(-\frac{a}{2} t^2 + bt \right)$

Chirp-Prime: $S_*(t) = \exp\left[j\left(\frac{a'}{2} t^2 \right) \right]$

Pure-Cosine: $u(t) = \cos(bt)$

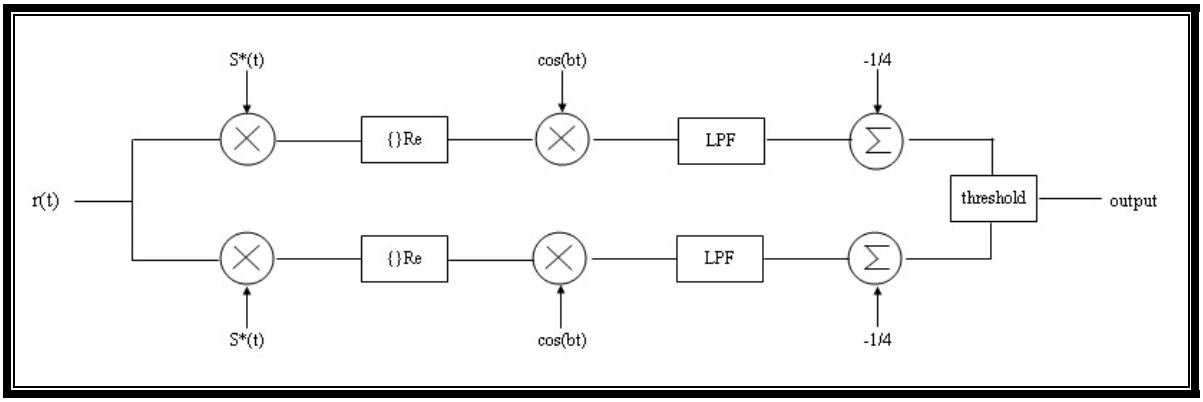

Figure 7.1 – Block diagram of the original model

Multiplication of chirp signals with chirp-prime:

Up-Chirp: $S_U S_* = \exp\left[j\left(\frac{a}{2} t^2 + bt \right) \right] \cdot \exp\left[j\left(\frac{a'}{2} t^2 \right) \right]$

$$= \exp\left[j\left(\frac{a}{2} t^2 + bt \right) + j\left(\frac{a'}{2} t^2 \right) \right]$$

$$S_U S_* = \exp\left[j\left(\frac{a + a'}{2} t^2 + bt \right) \right]$$

Down-Chirp: $$S_D S_* = \exp\left[j\left(-\frac{a}{2} t^2 + bt \right) \right] \cdot \exp\left[j\left(\frac{a'}{2} t^2 \right) \right]$$

$$= \exp\left[j\left(-\frac{a}{2} t^2 + bt \right) + j\left(\frac{a'}{2} t^2 \right) \right]$$

$$S_D S_* = \exp\left[j\left(\frac{-a + a'}{2} t^2 + bt \right) \right]$$

Because of the orthogonality of cos(x) and sin(x), analyzing only the real part or the imaginary part of the system is sufficient.

If $a' = -a$ $$S_U S_* = \exp\left[j\left(\frac{a - a}{2} t^2 + bt \right) \right]$$

$$= \exp[jbt] = \cos(bt) + j\sin(bt)$$

$$\mathrm{Re}\{S_U S_*\} = \cos(bt)$$

$$S_D S_* = \exp\left[j\left(\frac{-a - a}{2} t^2 + bt \right) \right]$$

$$= \exp\left[j\left(-at^2 + bt \right) \right] = \cos\left(-at^2 + bt \right) + j\sin\left(-at^2 + bt \right)$$

$$\mathrm{Re}\{S_D S_*\} = \cos\left(-at^2 + bt \right)$$

If $a' = a$ $$S_U S_* = \exp\left[j\left(\frac{a + a}{2} t^2 + bt \right) \right]$$

$$= \exp\left[j\left(at^2 + bt \right) \right] = \cos\left(at^2 + bt \right) + j\sin\left(at^2 + bt \right)$$

$$\mathrm{Re}\{S_U S_*\} = \cos\left(at^2 + bt \right)$$

$$S_D S_* = \exp\left[j\left(\frac{-a+a}{2} t^2 + bt \right) \right]$$

$$= \exp[jbt] = \cos(bt) + j\sin(bt)$$

$$\mathrm{Re}\{S_U S_*\} = \cos(bt)$$

Multiplying by the *u(t)*

<u>If a' = -a</u>

$$\mathrm{Re}\{S_U S_*\}\cos(bt) = \cos(bt)\cos(bt) = \frac{1}{2} + \frac{1}{2}\cos(2bt)$$

$$\mathrm{Re}\{S_D S_*\}\cos(bt) = \cos(-at^2 + bt)\cos(bt)$$

$$= \frac{1}{2}\cos(-at^2) + \frac{1}{2}\cos(-at^2 + 2bt)$$

<u>If a' = a</u>

$$\mathrm{Re}\{S_U S_*\}\cos(bt) = \cos(at^2 + bt)\cos(bt)$$

$$= \frac{1}{2}\cos(at^2) + \frac{1}{2}\cos(at^2 + 2bt)$$

$$\mathrm{Re}\{S_D S_*\}\cos(bt) = \cos(bt)\cos(bt) = \frac{1}{2} + \frac{1}{2}\cos(2bt)$$

Apply lowpass filter by setting $f << 2b$

<u>If a' = -a</u>

$$LPF[\mathrm{Re}\{S_U S_*\}\cos(bt)] = \frac{1}{2}$$

$$LPF[\mathrm{Re}\{S_D S_*\}\cos(bt)] = \frac{1}{2}\cos(at^2) \to 0$$

<u>If a' = a</u>

$$LPF[\mathrm{Re}\{S_U S_*\}\cos(bt)] = \frac{1}{2}\cos(at^2) \to 0$$

$$LPF[\mathrm{Re}\{S_D S_*\}\cos(bt)] = \frac{1}{2}$$

7.2 ADDITIONAL MATH DERIVATIONS

Up-chirp signal:

$$y_u(t) = s_u(t)\breve{c} \quad = \cos\left(2\pi f_{\min} t + \pi\mu t^2\right)\cdot\cos\left(2\pi f_{\min} t + \pi\mu t^2\right) \tag{3.17a}$$

$$= \cos^2\left(2\pi f_{\min} t + \pi\mu t^2\right)$$

$$= \frac{1}{2} + \frac{1}{2}\cos\left(4\pi f_{\min} t + 2\pi\mu t^2\right)$$

$$y_u(t) \quad = \frac{1}{2} + \frac{1}{2}\left[\cos\left(4\pi f_{\min} t\right)\cos\left(2\pi\mu t^2\right) - \sin\left(4\pi f_{\min} t\right)\sin\left(2\pi\mu t^2\right)\right] \tag{3.19a}$$

or equivalently

$$y_u(t) \quad = \frac{1}{2} + \frac{1}{2}\left[\cos\left(4\pi f_{\min} t\right)\cos\left(2\pi t^2\right) - \sin\left(4\pi f_{\min} t\right)\sin\left(2\pi t^2\right)\right] \tag{3.20a}$$

Down-chirp signal:

$$y_d(t) = s_d(t)\breve{c} \quad = \cos\left(2\pi f_{\max} t - \pi\mu t^2\right)\cos\left(2\pi f_{\min} t + \pi\mu t^2\right) \tag{3.17b}$$

$$= \frac{1}{2}\left[\cos\left(2\pi\left(f_{\max} - f_{\min}\right)t - 2\pi\mu t^2\right) + \cos\left(2\pi\left(f_{\max} + f_{\min}\right)t\right)\right]$$

$$= \frac{1}{2}\left[\cos\left(2\pi Bt - 2\pi\mu t^2\right) + \cos\left(2\pi\left(f_{\max} + f_{\min}\right)t\right)\right]$$

$$y_u(t) \quad = \frac{1}{2}\left[\cos\left(2\pi Bt\right)\cos\left(2\pi\mu t^2\right) + \sin\left(2\pi Bt\right)\sin\left(2\pi\mu t^2\right) + \cos\left(2\pi\left(f_{\max} + f_{\min}\right)t\right)\right] \tag{3.19b}$$

or equivalently

$$y_u(t) \quad = \frac{1}{2}\left[\cos\left(2\pi Bt\right)\cos\left(2\pi t^2\right) + \sin\left(2\pi Bt\right)\sin\left(2\pi t^2\right) + \cos\left(2\pi\left(f_{\max} + f_{\min}\right)t\right)\right] \tag{3.20a}$$

where $B = f_{\max} - f_{\min}$

7.3 BER VS. SNR TABLES

Table 7.1 – MODEL 1: BER vs. SNR table for simulation with Additive White Gaussian Noise (AWGN)

SNR (dB)	Variance, $\sigma^2(n_g)$	10 Errors	BER
1	100.0	26	3.85E-01
2	80.0	39	2.56E-01
2.5	70.0	39	2.56E-01
4	50.0	72	1.39E-01
5	40.0	98	1.02E-01
6	32.0	128	7.81E-02
7	25.0	183	5.46E-02
8	20.0	230	4.35E-02
9	16.0	395	2.53E-02
10	12.7	609	1.64E-02
11	10.1	1361	7.35E-03
12	8.0	3104	3.22E-03
13	6.4	8928	1.12E-03
14	5.1	22053	4.53E-04
15	4.0	120125	8.32E-05
16	3.0	1302412	7.68E-06
17	2.7	3749303	2.67E-06
17.4	2.3	26140065	3.83E-07

Table 7.2 – MODEL 2: BER vs. SNR table for simulation with Additive White Gaussian Noise (AWGN) and multipath

SNR (dB)	Variance, $\sigma^2(n_g)$	10 Errors	BER
3	62.80	24	4.17E-01
4	49.88	39	2.56E-01
5	39.62	41	2.44E-01
6	31.47	72	1.39E-01
7	25.00	103	9.71E-02
8	19.86	147	6.80E-02
9	15.77	195	5.13E-02
10	12.53	243	4.12E-02
11	9.95	415	2.41E-02
12	7.91	761	1.31E-02
13	6.28	1605	6.23E-03
14	4.99	3082	3.24E-03
15	3.96	9487	1.05E-03
16	3.15	38007	2.63E-04
17	2.50	194279	5.15E-05
18	1.99	658612	1.52E-05
19	1.58	6150523	1.63E-06
20	1.25	61319553	1.63E-07

Table 7.3 – MODEL 3: BER vs. SNR table for simulation with Additive White Gaussian Noise (AWGN) and Rayleigh amplitude fading

SNR (dB)	Variance, $\sigma^2(n_g)$	10 Errors	BER
0.97	100	27	3.70E-01
1.43	90	44	2.27E-01
1.94	80	45	2.22E-01
2.52	70	50	2.00E-01
3.19	60	55	1.82E-01
3.98	50	58	1.72E-01
4.44	45	67	1.49E-01
4.95	40	68	1.47E-01
5.53	35	73	1.37E-01
6.20	30	82	1.22E-01
6.99	25	97	1.03E-01
7.96	20	125	8.00E-02
9.21	15	133	7.52E-02
10.97	10	200	5.00E-02
11.43	9	295	3.39E-02
11.94	8	358	2.79E-02
12.52	7	583	1.72E-02
13.19	6	850	1.18E-02
13.98	5	1233	8.11E-03
14.95	4	3141	3.18E-03
16.20	3	10863	9.21E-04
17.96	2	57694	1.73E-04
20.97	1	17675985	5.66E-07

Table 7.4 – MODEL 4: BER vs. SNR table for simulation with Additive White Gaussian Noise (AWGN), Rayleigh amplitude fading, and multipath

SNR (dB)	Variance, $\sigma^2(n_g)$	10 Errors	BER
2	79.06	29	3.45E-01
3	62.80	43	2.33E-01
4	49.88	46	2.17E-01
5	39.62	61	1.64E-01
6	31.47	68	1.47E-01
7	25.00	97	1.03E-01
8	19.86	106	9.43E-02
9	15.77	125	8.00E-02
10	12.53	142	7.04E-02
11	9.95	174	5.75E-02
12	7.91	325	3.08E-02
13	6.28	436	2.29E-02
14	4.99	575	1.74E-02
15	3.96	898	1.11E-02
16	3.15	2485	4.02E-03
17	2.50	4985	2.01E-03
18	1.99	29429	3.40E-04
19	1.58	113370	8.82E-05
21	1.00	989063	1.01E-05
22	0.79	17869149	5.60E-07
23	0.63	50257043	1.99E-07

8. VITA

Lastri L. E. Simanjuntak was born on November 27, 1979 in Cairns, Australia, the daughter of Mr. & Mrs. Morison B. Simanjuntak. She graduated from The Long Trail School in Dorset, Vermont, in June 1998. She then attended the University of New Orleans, where she received her Bachelor of Science degree in Electrical Engineering in December 2002. She expects to receive her Master of Science degree in Engineering, with concentration in Electrical Engineering, in December 2004.